National University of Science and
Technology POLITEHNICA Bucharest

Doctoral School of Engineering and Applications of Lasers and Accelerators

Ph.D. Thesis
Summary

Alexandru MĂGUREANU

DEVELOPMENT OF SOLID TARGETS FOR FEMTOSECOND LASER DRIVEN PARTICLE AND RADIATION SOURCES

Dezvoltarea de ținte solide ca surse de particule și radiații acționate cu lasere de femtosecunde

---

CS1. Dr. Cătălin Mihai TICOȘ
Politehnica Univ. of Bucharest

PhD Supervisor

BUCHAREST 2025

DEVELOPMENT OF SOLID TARGETS FOR FEMTOSECOND LASER DRIVEN PARTICLE AND RADIATION SOURCES

Ph.D. Candidate
Alexandru MĂGUREANU

Scientific Coordinator
Sci. Researcher I, Dr. Cătălin M. TICOŞ

– Bucharest, 2025. –

Acknowledgements

This thesis is the result of the collective efforts, guidance, and support of many individuals and institutions, to whom I am deeply indebted.

I express my deepest gratitude to my Ph.D. supervisor, Dr. Cătălin Ticoș, for his mentorship, encouragement, and invaluable guidance throughout the development of this work. I am equally thankful to Dr. Valentin Crăciun for his constant guidance and for his essential contributions to target fabrication and characterization, to Dr. Călin A. Ur for his scientific advice, opportunities, and resources that made ELI-NP an outstanding environment for professional development, and to Dr. Daniel Ursescu for his insights on laser improvements and their relevance to our experiments.

I also wish to acknowledge my colleagues from the LDED department at ELI-NP for their collaboration and professionalism, with special thanks to Dr. Lucian Tudor, Dr. Viorel Năstasă, Dragana B. Dreghici, Matei Tătaru, Dr. Septimiu Bălășcuță, Mircea Pătrășcoiu, Dr. Ana M. Lupu, Dr. Bogdan Diaconescu, Dr. Dan Ghiță, Daniel Dorobantu, Diana Naum, and Rareș Iovanescu, as well as to Dr. Mihail Cernaianu, Dr. Petru Ghenuche, Dr. Marius Gugiu, Dr. Theodor Asavei, Dr. Deepak Sangwan, and Dr. Klaus Sphor for their support in experiments and practical problem-solving. My thanks also go to the theory group, Dr. Vojtech Horny, Bogdan Corobean, Dr. Chieh Yang and Dr. Paolo Tomassini, for stimulating discussions on foam physics. I am particularly grateful to Dr. Domenico Doria for his guidance in the laboratory and for involving me in numerous experiments at ELI-NP and abroad.

My appreciation extends to the Target Laboratory team, Dr. Cosmin Jalbă, Dr. Cristina Gheorghiu, Daniel Popa, Adrian Vatcu, and Dr. Victor Leca—for their advice and support in mounting Al targets. I also acknowledge the Laser Team at ELI-NP, with special thanks to Dr. Ioan Dăncuș, Andrei Nazîru, Lidia Văsescu, Saidbek Norbaev, Antonia Toma and Dr. Gabi Cojocaru, for the delivery of high-quality beams, as well as to Dr. Gabriel Bleotu and Dmitrii Nistor for their fruitful collaboration in experiments.

I am grateful to Professor Kazuo Tanaka for insightful discussions and recommended readings, and to Dr. Dan Stutman for valuable advice and for opening new perspectives beyond this research. I also acknowledge the Radioprotection team at ELI-NP, particularly Dr. Iani Mitu and Mara Popovici, for their support in experimental setups and ion monitoring, as well as the LGED team, particularly Dr Ovidiu Tesileanu, the group's head, and Dr. Liviu Neagu, for the collaborative experimental work we carried out.

Special thanks go to the INFLPR team, especially Dr. Gabriela Dorcioman, Dr. Petronela Garoi, and Dr. Doina Crăciun, for their collaboration in fabricating porous carbon foams and SEM

analysis. I am also indebted to the IFIN-HH team at Tandem, particularly Dr. Decebal Iacob and Dr. Diana Maria Mihai, for their help with n-RBS investigations, and to the Target Laboratory at IFIN-HH, especially Dr. Nicoleta Florea and Dr. Andreea Mitu, for their support in providing aluminium substrates for experiments in Japan.

My thanks extend to my international collaborators: the Astra-Gemini team—Dr. Hamad Ahmed, Daniel Molloy, Adrian McCay, and Dr. Lorenzo Romagnani—for their invaluable assistance during experiments at RAL; to Prof. Dr. Olga Rosmej and Parysatis Tavana, who invited me to the PHELIX experiment in Germany, where I acquired new diagnostic skills; and to Dr. Yuji Fukuda and Dr. Tatiana Pikuz for inviting me to participate in experiments at the J-KAREN laser in Japan.

I am profoundly thankful to my friends—Ioan and Ioana Ghițiu, Andrei and Teodora Madgearu, Ana Dobrin, Raluca Barbu, Ioana Puiu, Mircea Florea, Matei and Gabi Alexandru, Ioan Bulgaru, and many others—for their friendship and countless moments of joy.

Finally, to my family: thank you. To my wife, Natalia, for her unwavering love and support through every challenge and joy; to our daughter, Flavia, for the new dimension of happiness she brings into our lives; and to my parents, Malvina and Tiberiu Măgureanu, and my brother, Andrei Măgureanu, for their constant support, love, and nurturing presence.

Contents

Introduction

For some years, the rapid advancement of high-power laser technology has enabled a paradigm shift in particle acceleration research, transitioning from conventional radio-frequency accelerators toward the emerging field of laser-driven plasma acceleration [1], [2], [3]. This new approach exploits the extremely high energy densities achievable with femtosecond laser pulses, which facilitate the generation of ultra-strong electromagnetic fields during their interaction with solid targets [4]. These fields can accelerate particles to high energies over micrometre-scale acceleration distances [5], [6]. Unlike conventional accelerators, where the maximum achievable accelerating gradients are fundamentally linked to the vacuum breakdown within the accelerating structures (typically a few tens of MV/m), laser-driven acceleration exploits plasma as the acceleration medium. Being fully ionized, plasma can support field gradients exceeding several TV/m. In this context, the strength and efficiency of the accelerating field are predominantly governed by two factors: laser intensity and structural and material characteristics of the target.

Within this broader framework, the present thesis specifically addresses the advancement of solid target engineering for optimized proton acceleration via femtosecond laser-plasma interactions. The research focuses on the design, fabrication, and characterization of double-layer foam targets (DLFTs), consisting of an ultra-low-density carbon foam layer deposited on a solid aluminium foil substrate, alongside with the experimental validation of the target under femtosecond laser irradiation, for proving protons acceleration capabilities. To rigorously evaluate the performance of the proposed DLFTs, comparative studies were conducted using standard reference targets consisting of bare aluminium foils. Experimental campaigns covered an extensive set of beam intensities, from 10^{13} W/cm^2 to over 10^{21} W/cm^2, under both high-contrast and low-contrast conditions (with a high intensity prepulse preceding the main pulse by tens of nanoseconds). The coupling efficiency between the ultra-intense femtosecond laser pulses and the DLFTs was investigated in detail, with clear evidence demonstrating that the DLFTs significantly enhance proton acceleration compared to conventional foil targets.

The investigated topic, the advancement of structured targets for improving the particle acceleration, is of high importance for high-power laser-plasma interactions and its applications: compact particle accelerators, inertial confinement fusion, and medical therapies (e.g., proton therapy). The development of optimized targets is currently one of the major impediments to the practical implementation of laser-driven ion sources. Given the increasing accessibility of ultra-intense laser facilities (e.g., ELI [7], [8], [9], RAL [10], Apollon [11], Phelix [12], CoReLS [13], J-Karen [14], Bella [15] etc), there is a pressing need for target designs that are efficient for acceleration [16]. The double-layer foam targets developed and experimentally validated in this thesis represent a state-of-the-art contribution to ongoing research efforts aimed to enhance laser-driven proton acceleration for achieving higher proton energies, improved beam collimation, and shot-to-shot reproducibility. The utilization of these targets offers several benefits, including their cost-effectiveness and adaptability, making them suitable for a broad spectrum of experimental conditions, such as variations in laser intensity and temporal contrast.

The general objective of the thesis is to design, fabricate, and characterize advanced solid targets with enhanced performance for ultra-fast, femtosecond laser-based acceleration of protons, and to experimentally validate their effectiveness using an extensive set of beam intensities and contrast settings. This goal is addressed through a set of specific objectives, each directly corresponding to the content of the thesis chapters.

Chapter 1

Theoretical Background

1.1. Laser-Matter Interaction for Particle Acceleration

1.1.1. Fundamentals of Laser-Plasma Interaction

To understand the essential parameters relevant to the interaction between a high-intensity focused laser beam and a target, it is necessary to define and discuss fundamental plasma properties.

The concept of plasma is central to laser-plasma acceleration. The most well-known definitions of plasma as ionized gas, comes from the one introducing the “plasma” term, I. Langmuir, 1928 who described it as “containing balanced charges of ions and electrons” [17], [18]. A more “useful” definition was provided by F. Chen [19] as a “quasineutral gas of charged and neutral particles which exhibits collective behaviour”.

Before elaborating on the quasineutral property, it is important to introduce the concept of temperature in plasmas, which relates directly to the kinetic energy of particles. In a gas at thermal equilibrium, particles exhibit a Maxwellian velocity distribution, and their average kinetic energy in a three-dimensional space is given by:

$$E_a = \frac{3}{2} K_B T \tag{1.1}$$

Each degree of freedom contributes to the kinetic energy $E_{av} = 1/2\, K_B T$, where $K_B = 1.38 \times 10^{-23} J/K$ represents the Boltzmann’s constant while T represents the temperature.

The “quasineutral” properties referred in Chen’s definition comes from the fact that the plasma shields out external electric potentials. Over sufficiently large volumes and time scales, a plasma tends to maintain nearly zero net charge. However, at smaller scales, local charge imbalances can occur, giving rise to electric fields. The distance at which the plasma neutralises any distinct charge is defined as the Debye length, λ_D:

$$\lambda_D \equiv \left(\frac{\varepsilon_0 k_B T_e}{n_e e^2}\right)^{1/2} \tag{1.2}$$

with n_e being electron density while T_e represents electron temperature.

After this general introduction of the fundamental parameters in plasma, we can approach the electrons behaviour in plasma under laser irradiation. In an energized plasma where the laser strips electrons from the quasi-stationary ions, the quasi-neutrality is restored through an electric field. This makes the electrons with density n_e to oscillate with respect to the ions at a frequency called plasma frequency (or Langmuir frequency)

$$\omega_P \ = \left(\frac{e^2 n_e}{\varepsilon_0 \bar{\gamma} m_e}\right)^{1/2} \tag{1.3}$$

where Lorentz factor $\bar{\gamma}$ is defined as $\bar{\gamma} \equiv \sqrt{1 \,/\, (1 - v^2/c^2)}$ with v being the electron velocity.

The laser matter interaction is greatly influenced by the plasma frequency. A high intensity laser (even at intensity of about 10^9 W/cm^2 [20]) can ionize the targets surfaces generating a plasma. The plasma starts to expand in vacuum producing a gradient of plasma density, which is associated with a gradient of plasma frequency.

If at a certain layer within this plasma gradient the local plasma frequency ω_P exceeds the laser frequency ω_L, the electrons are able to create electric currents that will screen the fields of the laser EM wave [21]. Thus, the laser can no longer be transmitted and causes the incident beam to be reflected by the plasma. Such plasmas are known "overdense" or "overcritical". Assuming an exponentially decaying of the amplitude of the laser wave, the laser can penetrate rapidly decaying to over a very limited distance, known as the skin depth l_s and defined as:

$$l_s = \frac{c}{\sqrt{\omega_P^2 - \omega_L^2}} \tag{1.4}$$

The lasers can propagate through the plasma only when $\omega_L > \omega_P$. Under these conditions, the plasma is considered "undersense" or "undercritical".

The case when $\omega_L = \omega_P$ defines a density regime called critical plasma density, n_c:

$$n_C = \frac{\varepsilon_0 m_e \omega_L^2}{e^2} \tag{1.5}$$

At this density, the plasma's refractive index is

$$\eta = \left(1 - \frac{\omega_p}{\omega_L}\right)^{1/2} \tag{1.6}$$

If $n_e < n_c$ the laser can propagate through the plasma, while for $n_e > n_c$, it is reflected.

For large enough laser intensity, its electric field amplitude becomes so strong that it accelerates electrons to relativistic speeds and the electrons' mass increases (as described by the Lorentz factor $\bar{\gamma}$) in turn lowering the plasma frequency, increasing the critical density, hence allowing laser transmission through the plasma that was previously overdense. This regime is also called relativistic transparency and is observed in experiments when very thin targets with a nm scale size thickness are employed. The relativistic critical density $n_C^{relativist}$ is then:

$$n_C^{relativist} = \frac{\bar{\gamma}\varepsilon_0 m_e \omega_L^2}{e^2} \tag{1.7}$$

1.1.2. Laser driven ion acceleration from solid targets

The dynamics of laser–solid coupling under ultra-intense irradiation is characterised by a complex combination of electron heating mechanisms (whose relative contributions depend strongly on the laser characteristics, focused beam intensity, incidence angle, polarisation state, but also on target characteristics, material composition but also plasma scale length).

This mechanism (i.e. vacuum heating and j × B heating) enables efficient coupling of laser pulse energy to hot relativistic electrons, which typically acquire average energies of several mega-electronvolts (MeV). Due to their relatively long collisional mean free paths, which substantially exceed the target thickness, they are capable of propagating through the target and reaching its rear surface. There, their attempt to escape the target establishes a space-charge field, that drives the acceleration of the ions on the back (rear) target surface [22].

This process results in the production of quasistatic electric fields in the plasma, with field strengths reaching several GV/µm, or equivalently, teravolts per meter (TV/m). These fields vastly exceed the limits attainable by conventional radiofrequency-based acceleration technologies, which are typically constrained to tens of megavolts per meter (MV/m) [21], [23]. Ions gain energy in this field, originating from the ponderomotive potential. This leads to a rapid expulsion of ions, which can acquire energies to about tens of MeV [24].

The acceleration mechanism driven by this charge separation field is known as Target Normal Sheath Acceleration (TNSA).

Target Normal Sheath Acceleration

The Target Normal Sheath Acceleration (TNSA) mechanism is the most extensively studied and experimentally validated approach for ion acceleration using high-intensity laser pulses [3], [22],

[25], [26]. It relies on ions originating from hydrogen-rich contaminants naturally present on the rear (non-irradiated) surface of micrometre-thick solid targets.

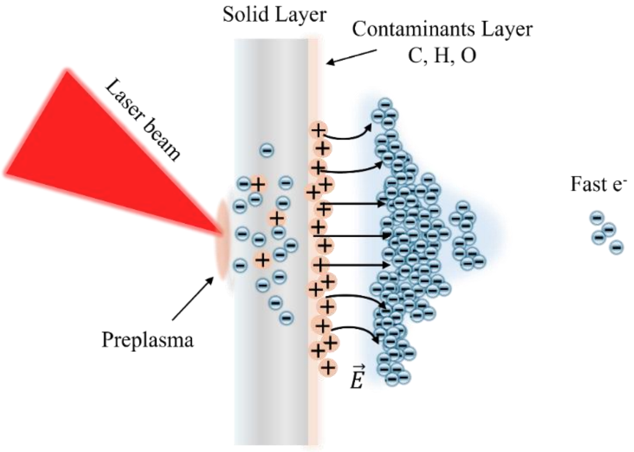

Figure 1.1. *Schematic representation of the target normal sheath acceleration (TNSA) process.*

When the leading edge of the laser pulse (pedestal or pre-pulses) interacts with the target front, a plasma is formed. The main laser pulse then heats electrons to relativistic energies, enabling them to propagate through the target bulk and, in some cases, escape from the rear surface into vacuum. This escape leaves behind a net positive charge that establishes a strong electrostatic restoring force. While lower-energy electrons are reflected within the target, the fastest electrons accumulate at the rear surface, stabilizing a quasi-static Debye sheath [27]. Hot electrons are therefore the key mediators, as their escape drives the formation of the sheath electric field, which in turn accelerates the ions.

The accumulation of fast electrons at the back surface results in the stabilization of a quasi-static electrostatic sheath, often referred to as a Debye sheath. The charge imbalance between the population of hot electrons forming the Debye sheath and the positive ions on the target rear surface, gives rise to an extremely strong electric field E_s, normal to the back surface of the target. The magnitude of this sheath field usually reaches values of about $10^{12}\ V/$ m and is sufficiently strong to rapidly ionize atoms from the layer of contaminants on the target surface or, in some cases, from within the target material itself. These ionized species are finally accelerated to high energies. Since the contaminant layer consists mainly of adsorbed hydrocarbons and water vapour, protons dominate the acceleration process. Their favourable charge-to-mass ratio and spatial location at the sheath peak allow them to achieve the highest velocities.

Ion beams generated via TNSA exhibit broadband, exponentially decaying energy spectra with a characteristic high-energy cut-off, a parameter commonly used to evaluate experimental performance and TNSA efficiency [22].

1.2. Experimental Methods and Diagnostics

1.2.1. Plasma Mirror and Laser Contrast

In laser systems reaching high power levels, most of the beam energy is typically confined to the ultra-fast pulse duration of the main beam. However, a non-negligible fraction of the total energy is temporally distributed outside the main peak, forming a background structure composed of a low-intensity pedestal and distinct intensity modulations known as pre-pulses. These temporal features are illustrated in Figure 1.2, which depicts a representative temporal intensity profile at picoseconds timescale.

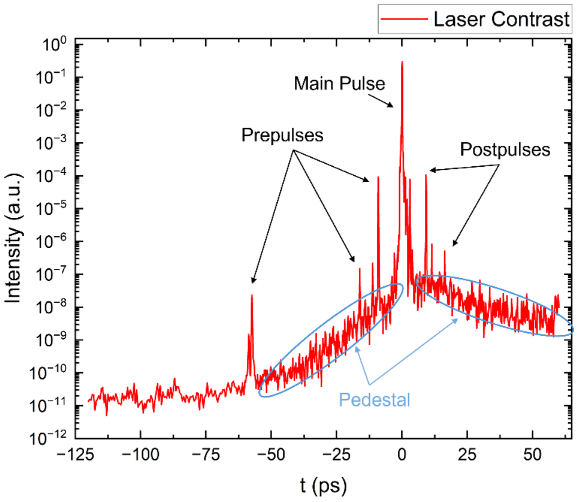

Figure 1.2. *Representative intensity contrast in picoseconds scale timeframe, for a high-power laser, highlighting the main features of the spectrum: the main pulse, the pre-pulses, the post-pulses and the laser pedestal.*

The temporal contrast of a laser system is determined by the ratio of the peak intensity of the main beam to the intensity of the background light, including both the pedestal and any pre-pulses. Accurate optimisation and characterisation of the contrast are necessary for experiments involving laser matter interaction for ion acceleration.

Pre-pulses preceding the main pulse are of particular concern, as they can induce significant pre-expansion of the target. Low temporal contrast, corresponding to intense prepulses, can lead to the formation of an extended preplasma with a scale length that can negatively impact the efficiency and quality of the ion acceleration process. High temporal contrast generally correlates with improved experimental outcomes, particularly for mechanisms such as TNSA [28], [29], [30]. However, the influence of prepulses is not always detrimental. Under certain experimental conditions, depending on the target structure and the dominant acceleration mechanism, preplasma formation induced by controlled prepulses can enhance the acceleration process [31], [32]. Therefore, understanding and tailoring the temporal contrast of high-power laser pulses is fundamental to the design and interpretation of such experiments.

Plasma Mirror

A widely adopted technique for enhancing the temporal contrast of high-power laser systems and suppressing undesired prepulses is the implementation of a plasma mirror (PM). The plasma mirror functions as an intensity-dependent optical element, typically based on an anti-reflective dielectric-coated substrate. It exploits the nonlinear reflectivity of the surface: at low intensities (e.g., those associated with the pedestal, or prepulses), the surface remains nearly transparent for the incident radiation; however, when the intensity exceeds a critical threshold, typically reached by the main pulse, the surface undergoes rapid ionization, forming a dense plasma that acts as a high-reflectivity mirror. This mechanism allows the plasma mirror to suppress low-intensity background components while efficiently reflecting the high-intensity main pulse toward the target, significantly improving the temporal intensity contrast on target [33].

A schematic representation of a Plasma Mirror functioning principle is presented Figure 1.3.

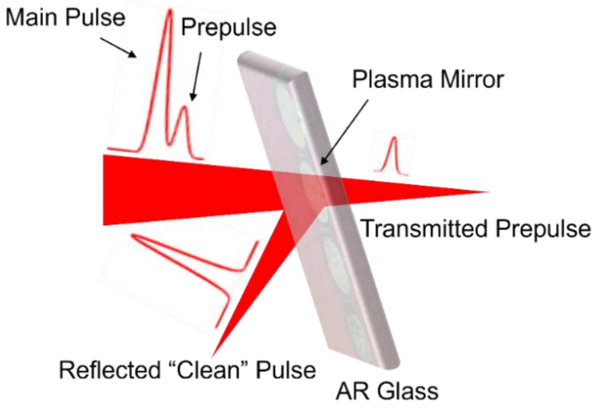

Figure 1.3. *Schematic representation of a Plasma Mirror working principle*

Beyond contrast enhancement, plasma mirrors also play a crucial role in attenuating back reflected light from the interaction point [34], which is essential for protecting optical components, including the final compressor gratings and amplification stages, from potential damage. A geometrical model for plasma mirror alignment in high-power laser experiments.

1.2.2. Plasma Imaging Diagnostics

Plasma imaging diagnostics are essential for understanding laser-driven plasma dynamics in experiments with high-power lasers. Imaging the plasma produced by ultrashort laser pulses focused into a solid target is an essential diagnostic technique. The shadowgraphy approach is a robust, straightforward technique where a probe beam extracted from the main laser beam illuminates from a side the plasma plume created by the focused laser as it ionises the solid target.

[35], [36], [37]. Illuminating the target from a side produces a shadow image of the interaction, which is then recorded by a CCD camera. Accurate alignment of the pulsed main beam with the probe beam is essential for the imaging process, requiring precise spatial and temporal synchronisation between the two beams.

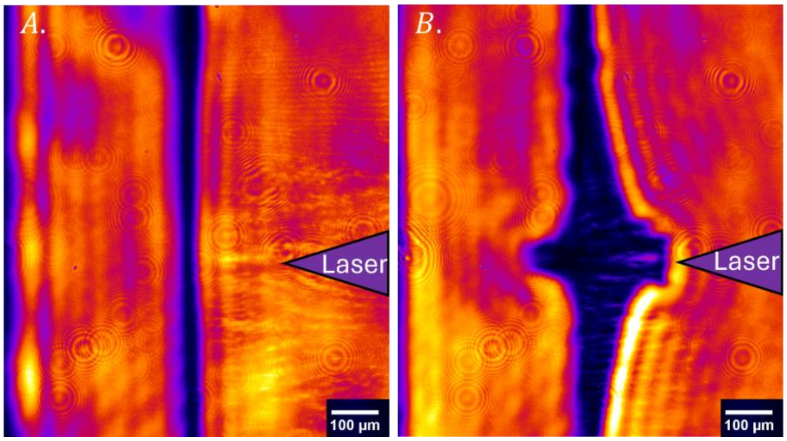

Figure 1.4. *Shadowgraphy picture (or side view picture) of the Aluminium thin foil target at different moments, A. 20 ps prior to interacting with the main laser pulse (i.e., -20 ps) and B. after (i.e., at +200 ps) interacting with the main laser pulse*

1.2.3. Ion Diagnostics

Ion beam characterization in this work relied on three complementary diagnostic techniques: the Thomson Parabola Spectrometer (TPS), Time-of-Flight (TOF), and Radiochromic Films (RCFs). The TPS provides high-resolution, species-specific energy spectra by exploiting the distinct deflections of ions in orthogonal electric and magnetic fields, producing characteristic parabolic traces for each charge-to-mass ratio. TOF diagnostics enable real-time measurements of ion energies, flux, and species composition by correlating ion arrival times with a reference photo-peak signal from prompt electromagnetic emission. RCF stacks, based on the Bragg peak energy deposition, offer a robust and spatially resolved method to reconstruct proton spectra and beam profiles, with optical density changes serving as a proxy for absorbed dose. Combined, these diagnostics allow for both qualitative and quantitative assessment of the spectral, spatial, and temporal features of laser-accelerated ion beams**.**

Chapter 2

Targets for laser driven proton acceleration based on TNSA

This chapter presents a comprehensive study reviewing the main results obtained in the field of proton acceleration from solid targets, with the objective of identifying the most suitable target for enhancing laser-driven proton acceleration via the Target Normal Sheath Acceleration (TNSA) regime. The core content of this chapter has been extensively detailed in a scientific paper, in which I am the first author [38].

The majority of early experiments have been performed with flat foil targets, with the dominant acceleration mechanism identified as Target Normal Sheath Acceleration (TNSA). In this regime, electrons accelerated by the incident high-intensity laser pulse traverse the target and create a spatial charge very close to the backside of the target, resulting in the acceleration of protons and ions [25]. The temperature of the escaping electrons resulting from the generated plasma has been found to be a key parameter in this process.

TNSA remains the most widely used laser-driven ion acceleration mechanism, mainly due to its high reproducibility and relative experimental simplicity. Due to its robustness and scalability, it remains one of the most promising candidates for practical implementation in the next generation of laser-driven proton acceleration applications.

In pursuit of a unified strategy to address these challenges, i.e. enhance electron heating, minimise laser reflection and increase surface electron density, numerous target surface morphologies have been proposed and investigated. Among these, the incorporation of nanostructures such as nanospheres, nanorods, micropillars, low-density foams and surface-embedded gratings has shown promise in improving the efficiency of laser-matter coupling. These structural modifications allow for more efficient absorption of laser energy and improved generation of hot electrons, which are critical for driving high gradient sheath fields.

Aluminium is one of the most widely used materials for the fabrication of laser-driven proton accelerator targets. Some of the first experimental results in this field were obtained using thin Al films [39], [40], [41], [42].

Additional experiments have investigated the use of various metallic foils as target materials, but there is no clear correlation between the type of metal and a systematic increase in proton energy. However, the highest recorded energies from various metallic foils (except from Al foils), approaching 60 MeV, - have been achieved using Mo, Au, Fe and SS targets (Mo, 58.5 MeV [43]**;** Au, 50 MeV [44]**;** Fe, 42 MeV [45]**;** , SS, 40 MeV [46]).

One of the earliest significant results in laser-driven proton acceleration, which remained a benchmark for several years, reported a maximum proton energy of 58 MeV obtained from a 100 µm thick polystyrene (PS) foil target [4]. Other results included polystyrene (PS) foils [4], [5], [47], [48], [49], [50], Mylar (polyethylene terephthalate) [39], [51], [52], [53], [54], [55], [56], polymethylpentene (PMP) [44], Kapton [57], as well as other non-metallic substrates such as silicon nitride (Si_3N_4) [54], [55], [56], [57], [58], amorphous carbon [59] and chemical vapour deposited (CVD) synthetic diamond [60]. In addition, results on more unconventional materials - such as the liquid crystal- 8CB [61] and pure silicon substrates [62] - are included to highlight the range of target materials being explored in the effort to optimize proton acceleration.

A comparative analysis of the different target configurations is presented in Figure 2.1, focusing on a narrow laser pulse duration window, approximately 25 to 45 femtoseconds, with a fixed central wavelength of 800 nm. The observed trends in maximum proton energies are consistent with previous results, with the data naturally clustering into two distinct regimes based on laser intensity, as shown in Figure 2.1

In the lower intensity regime ($\lesssim 4\times10^{19}$ W/cm^2), the cut-off energies remain relatively modest - typically in the range of a few MeV - and show limited variation across different target morphologies. Notable exceptions include a submicron aluminium foil, which yielded a proton energy peak of 11 MeV under conditions of ultrahigh temporal contrast (10^{-10}) [63]. However, for most targets in this intensity range, nanostructuring of the surface - via the incorporation of micro- or nanospheres, nanowires or nanoholes - does not result in a significant increase in proton acceleration.

Contrarily, in the higher intensity regime ($\gtrsim 5\times10^{19}$ W/cm^2), a broader distribution of peak proton energies is observed. The most prominent result is a 60 MeV cut-off obtained using a double-layer target coated with a foam layer [64], followed by a 29 MeV cut-off from a similarly structured foam target [65]. Interestingly, despite the improved microstructure, these values remain below those obtained with selected aluminium foils, which reach up to 40 MeV [46], [66]. It is important to note that all four of these high energy cases were achieved under conditions of high temporal contrast, reaching up to 10^{-11} for the foam-based targets.

Double-layered targets generally produce proton energies in the 10-20 MeV range, especially when the thicknesses are in the micrometre range or below. However, improvements in laser contrast (from 10^{-6} to 10^{-10}) do not appear to translate into significant performance gains in this case.

When considering the influence of pulse duration (Figure 2.1) the foam-based targets that achieved the highest energies were irradiated with ultrashort pulses of 30 fs, while their aluminum counterparts were exposed to slightly longer pulses of 45 fs. Most of the nanostructured targets were evaluated within an intermediate pulse duration range of 30-35 fs, suggesting that the optimal conditions for maximum energy gain may depend not only on the target morphology and laser intensity, but also on the fine tuning of the temporal characteristics of the driving pulse.

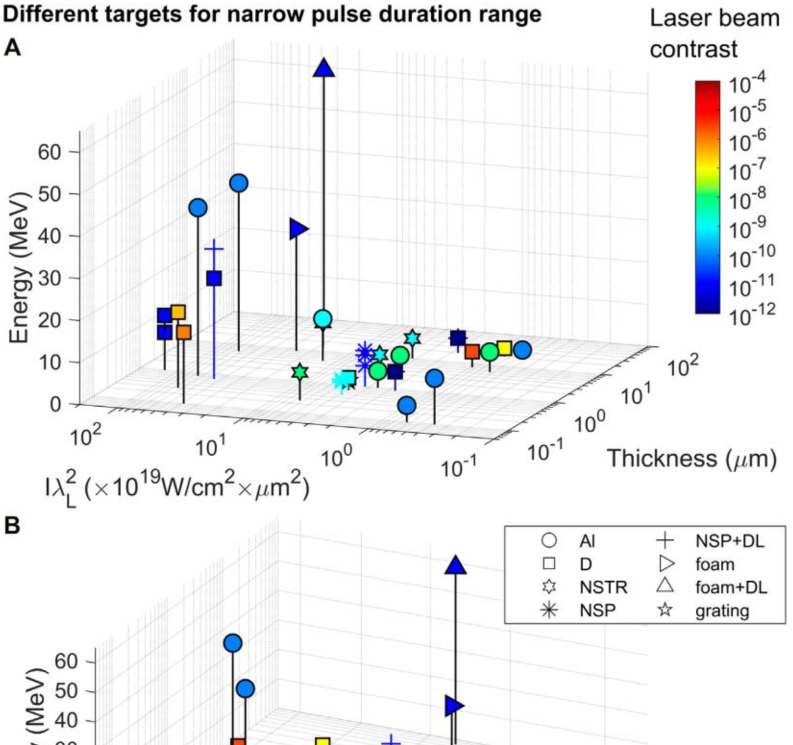

Figure 2.1. *Maximum energy of protons accelerated from different target types: (A) vs. product of laser intensity and squared laser wavelength* $I\lambda_L^2$ *and target thickness, and (B) vs. laser pulse duration and target thickness. The targets are Al foils "Al" (40 MeV [46], [66], 11 MeV [63], 10 MeV[67], 4.8 MeV [68], 4.5 MeV [69], 4 MeV[28], [69], 0.6 MeV [28], dielectric and non-metallic foils "D", i.e, Mylar (24 MeV [56], 9 MeV[54], 3.5 and 4.5 MeV [55], 2 MeV [52]), Kapton (3.8 MeV[57]), SiN (13 MeV [54], 3 MeV [58]), liquid crystal (18 MeV [61]) and amorphous carbon (17 MeV [59]), nano- and microstructured films "NSTR", i.e, nanowires (4.8 and 5.6 MeV [70]), nanoholes (6.7 MeV[71]), nanochannels (6 MeV [72]), nanospheres "NSP"*

(5, 7.5 and 8.6 MeV[73], 3.5 and 4.5 MeV [55], 3 and 3.6 MeV[58]), nanospheres on a double layer target "NSP + DL" (31 MeV [56]), "foam" target (29 MeV [65]), foam with double layer "foam + DL" (60 MeV [64]) and "gratings" (2.3 MeV [58]). The colour bar shows the laser contrast for each data point. The contrast values are given in the above references, typically for a few picoseconds or tens of picoseconds before the main pulse.

After analysing all these types of targets we propose that the most suitable target for the purpose of enhancing the acceleration of the protons would be a double layer foam target (DLFT) consisting of an ultra-low density layer on top of an Aluminium Layer. The low density structure can lead to the formation of a controlled near-critical plasma layer on the illuminated side, allowing the laser pulse to penetrate deeper into the target. This can favour an enhanced laser energy absorption within a larger plasma volume and a more efficient heating of the electrons, improving the conditions for ion acceleration [64], [65]. The Al layer is one of the most benchmarked materials used for target fabrication.

Chapter 3

Development of Double Layer Foam Targets for Proton acceleration

As shown in the Chapter 2, a double-layer foam target (DLFT) consisting of an ultra-low-density Carbon layer deposited on aluminium foil was identified as one of the most effective designs for enhancing laser-driven proton acceleration. This chapter comprehensively explains the steps for manufacturing and characterizing such structured targets.

3.1. Designing the targets for the experiment

For accelerating the protons in the TNSA regime I identified from multiple scientific studies[65] [74] [64] that double-layer foam target (DLFT), consisting of an ultra-low density Carbon layer deposited on Aluminium foils, is one of the most effective. The solid layer containing the Al foil should have a thickness between hundreds of nanometers to few microns while the ultra-low density Carbon layer should have a thickness in the order of microns to tens of microns and a density in the range of 5 to 30 mg/cc.

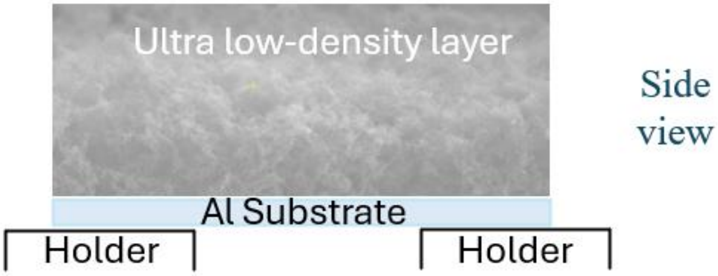

Figure 3.1. *Schematic side-view representation of the designed DLFT, illustrating the ultra-low-density carbon layer deposited to an Al substrate, mounted on the target supporting holders.*

In the schematic representation of the DLFT presented in Figure 3.1., an ultra-low-density carbon foam (density of a few mg/cc) is deposited onto a solid Al foil. The Al layer was used on the backside of this target. The Al thickness ranges is 0.4, 0.8, 1.5, 3, 4.5, 6, 10 microns. The ultra-thin layers 0.4 and 0.8 allow faster electron transport through the substrate, enabling the generation of a strong sheath field at the rear surface with lower energy losses and the thicker one, from 1.5 to 10 microns, have a better structural stability. All these thicknesses are commonly used in laser-plasma experiments with Al foils.

Carbon was used for the ultra-low density layer (Foam Layer), in the front side of the target, because it has a low atomic number, Z which reduces energy losses due to Bremsstrahlung radiation, ensuring that more of the laser energy is converted into heating electrons rather than being emitted as X-rays. Carbon foams are highly porous with densities that can be adjusted within a few to tens of mg/cc range.

3.2. Fabrication and Deposition Techniques

In order to develop such an ultra-low density carbon layer, the Pulse Lased Deposition (PLD) technique was involved. PLD allows precise control over the thickness, density, and morphology of the carbon layer and can lead to the formation of a C layer with a density in the range of mg/cc. The production of ultra-low-density C layers or C foam using PLD relies on the aggregation of ablated carbon clusters in a controlled gas environment. Carbon nanofoams are highly porous, snow-like structures characterized by void fractions above 90%, composed of interconnected carbon nanoparticles. These foams possess unique properties, such as high surface-to-volume ratios, unusual electrical conductivity behaviour, and a mixture of sp1, sp2, and sp3 hybridization states, making them attractive also for applications in catalysis, energy storage, and advanced coatings. The growth mechanism of C foams in PLD depends on several key parameters, including laser fluence, pulse duration, repetition rate, and background gas pressure. During ablation, carbon atoms and clusters are ejected from the target and undergo collisions with gas molecules in the deposition chamber. These interactions influence the cooling and aggregation dynamics of carbon species, promoting the formation of nanoparticle aggregates that eventually assemble into a three-dimensional porous network[75], [76]. The presence of background gas is crucial in determining foam morphology, as higher pressures lead to increased scattering and diffusion-limited aggregation, resulting in a more porous and interconnected structure [77] [78], [79], [80]. Low pressures favour ballistic transport and the formation of denser films, while higher pressures lead to enhanced nanoparticle interactions, promoting the development of ultra-low density foams.

For the deposition of the Carbon Foam layer in the DLFT, two distinct PLD systems were employed, each utilizing an excimer laser source with specific operational parameters. The first system featured a KrF* excimer laser (COMPex Pro 205) with at a wavelength of 248 nm and a full width at half maximum (FWHM) pulse duration of ≤25 ns. The laser operated at a repetition rate between 10 Hz and 40 Hz, delivering pulses with an energy of approximately 320 mJ, monitored using a Coherent measurement system. The second system utilized an ArF excimer laser with a wavelength of 193 nm, producing laser pulses with a duration of 25 ns at a repetition rate of 40 Hz, each pulse delivering 500 mJ of energy.

In both setups, the laser pulses were focused onto a bulk graphite target within a controlled low-pressure background gas environment. The deposition duration varied from 3 to 25 minutes. The laser beam in each system was directed into the target at an incidence angle of 45 degrees. The ablated material was ejected in a highly forward-directional manner, forming a narrow plasma plume where the substrate was positioned. To optimize deposition conditions and achieve the desired carbon foam properties, the target-to-substrate distance was adjusted between 5 cm and 7 cm in both cases.

Depositions were carried out in different background gases, specifically N_2, or CH_4 at pressures ranging from 1 mbar to 10 mbar. These gases were found to increase collision frequency and clustering effects, leading to the formation of highly porous carbon structures.

3.3. Characterisation

The first qualitative observation of the carbon foam layer integrated into the DLFT targets was made immediately after the deposition process, upon removal of the sample holder from the PLD chamber. It became instantly clear that the carbon foam had been deposited onto the designated substrates, but also across the entire mask assembly, including the openings, screws, and surrounding surfaces. Visually and texturally, the deposited material was similar to the fine, fluffy, loosely bound household dust that accumulates in corners. The structure appeared extremely fragile, tending to detach upon minimal contact.

To conduct a detailed evaluation of the target properties, we used scanning electron microscopy (SEM). SEM is a powerful technique that provides high-resolution imaging of surface morphology and near-surface microstructure. This makes it ideally suited to analyse the morphology, porosity and structural characteristics of the carbon foam.

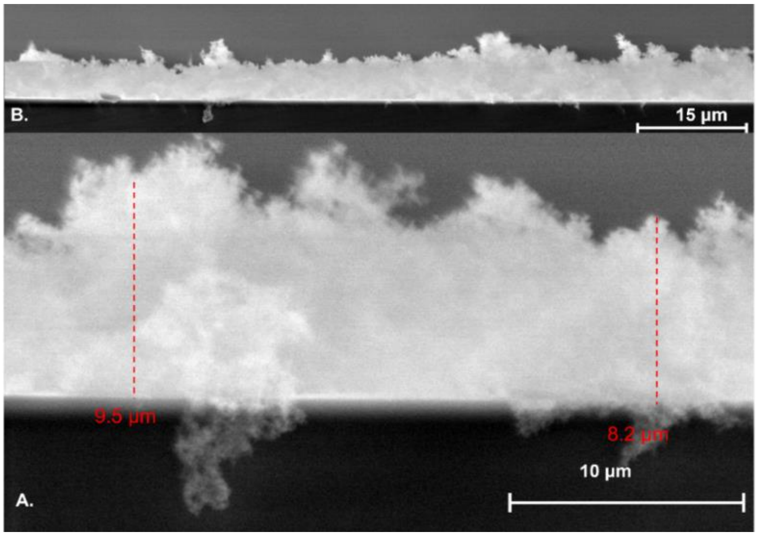

Figure 3.2. *Cross-sectional SEM images of a carbon foam layer deposited on a Si substrate using PLD at 310 mJ, 20 Hz, in 2 mbar CH_4 background gas for 5 minutes.* ***(A)*** *High-resolution zoom showing local thickness variation and target morphology.* ***(B)*** *Lower-magnification image displaying the overall thickness uniformity across a broader lateral area.*

Figure 3.2. presents cross-sectional SEM images of a C foam layer deposited on a Si substrate, taken at two different magnifications to highlight both local microstructural detail and overall thickness uniformity. These images offer valuable insight into the morphology, porosity, and thickness profile of the deposited foam, serving as strong visual evidence of its ultra-low-density nature. In Figure 3.2.A., a higher-magnification view captures a localized region of the C foam, clearly revealing the irregular topography characteristic of its porous structure. The foam thickness varies from approximately 8.2 µm to 9.5 µm, indicating localized non-uniformity due to the stochastic nature of plume dynamics during PLD. The surface of the foam exhibits a snowflake-like morphology, composed of loosely packed carbon structures. This morphology is a distinct feature of ultra-low-density C materials and differs considerably from that of compact or dense amorphous carbon films, which typically present sharp, planar interfaces and smooth surfaces.

The compositional analysis of the carbon foam (C foam) targets was carried out using X-ray Photoelectron Spectroscopy (XPS).

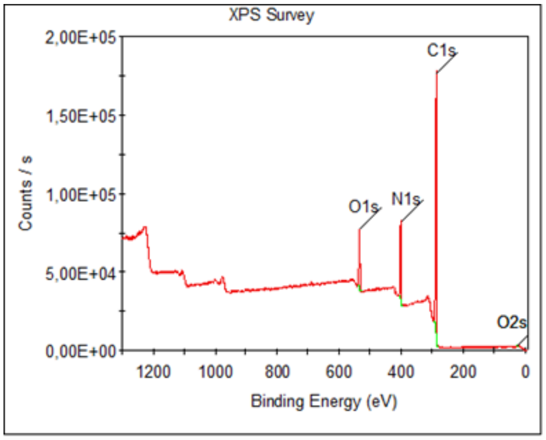

Figure 3.3. *XPS survey spectrum acquired from a foam deposited under 1 mbar of N2*

Figure 3.3. presents an X-ray Photoelectron Spectroscopy (XPS) survey spectrum of a carbon foam sample deposited under a nitrogen (N_2) atmosphere at a pressure of 1 mbar. Due to the high surface area of foam-like materials, a substantial amount of N_2 was adsorbed onto the surface, accounting for approximately 16.3% of the detected signal. The N 1s peak, located at a binding energy of 399.2 eV, is attributed to molecular nitrogen adsorbed into the foam structure. Additionally, exposure of the foam to ambient conditions led to the adsorption of oxygen (O_2) and water (H_2O), as evidenced by the presence of an O 1s peak at 532.1 eV, which corresponds to an oxygen content of 7.6%. These findings suggest a high surface-to-volume ratio, characteristic of materials with a high degree of porosity. When the deposition was conducted exclusively under a methane (CH_4) atmosphere, the XPS spectra showed only C 1s and O 1s peaks.

Non-Rutherford backscattering spectrometry (n-RBS) was employed to analyze the carbon foam layers deposited on silicon (Si) substrates. The measurements were conducted under high vacuum conditions (~10^{-6} mbar) using a 4.27 MeV He^{2+} beam delivered by a 3 MV Tandetron accelerator, with a duoplasmatron ion source. Backscattered alpha particles were detected by passivated ion-implanted silicon detector, placed at a backscattering angle of 165° relative to the incident beam.

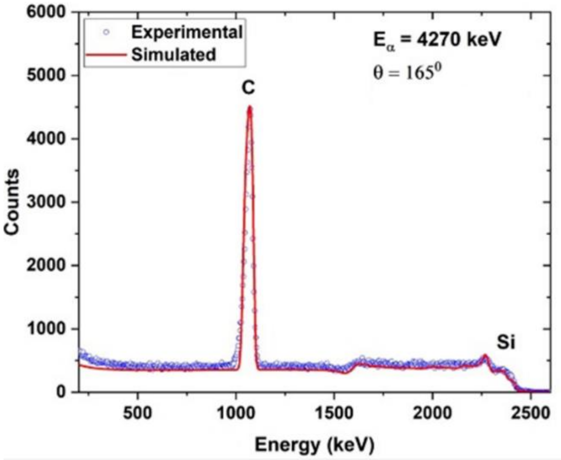

Figure 3.4. *N-RBS spectrum of a Carbon foam deposited on a Si substrate.*

Figure 3.4. displays a non–Rutherford Backscattering (n-RBS) measurement or nuclear resonance elastic scattering of a carbon foam deposited on a Si substrate. The simulated spectrum yielded an areal density of approximately: $A_\rho = 100 \times 10^{15}\ atoms/cm^2$.

Assuming a film thickness, t , of approximately 10 µm, as determined from SEM cross-sectional analysis, the mass density ρ of the carbon foam layer can be approximated by:

$$\rho = \frac{A_\rho}{t} \cdot m_C = \frac{10^3 \times 10^{15}\ atoms\ cm^{-2}}{10\ \mu m} \cdot 2 \times 10^{-23}\ g\ atom^{-1} = 20\ mg/cc \qquad (3.1)$$

where A_ρ is the areal density (atoms cm^{-2}), obtained from the nRBS spectrum fitting, t is the thickness of the C Foam, m_C is the mass of a single carbon atom, given by $m_C = \mu_c/N_A$, with $\mu = 12\ g/mol$ (molar mass of Carbon) and N_A = 6.022 × 10^{23} atoms/mol (Avogadro's number).

Quantitative measurements of the C foam density were performed using a high-precision microbalance. These gravimetric measurements indicate that the carbon foam density lies in the range of 5 to 30 mg/cc, depending on deposition parameters such as background gas pressure and deposition time. This density range is also in excellent agreement with the estimated density by NRBS. This range is approximately two to three orders of magnitude lower than that of compact amorphous carbon (~2.2 g/cm^3), confirming the formation of an extremely porous, ultra-low-density structure.

The gravimetric procedure consisted of precisely weighing the Si substrate before and after the deposition of the C foam. The mass difference corresponds to the net mass of the deposited foam. In combination with the optical imaging to estimate the coated area and cross-sectional SEM analysis to determine the foam thickness, an estimate of the foam volume was obtained. From the measured mass and calculated volume, the average bulk density of the carbon foam layer was derived.

These results are consistent with the estimated density from n-RBS measurements and with morphological evidence observed in SEM cross-sectional images, which reveal a snowflake-like microstructure composed of loosely connected carbon structures and high void volume fractions. The low apparent density is further supported by XPS surface analysis, which shows significant adsorption of oxygen and moisture from the ambient environment, characteristic behaviour of high-surface-area materials. Together, the gravimetric, n-RBS, SEM, and XPS analyses provide complementary insights that converge on the same conclusion: the carbon foam produced under PLD conditions forms a highly porous, low-mass-density material, suitable for advanced laser–plasma interaction.

Chapter 4

Experimental testing of the DLFT

After we present a detailed methodology for fabricating the DLFT consisting of an ultra-low density carbon layer on a thin foil Al substrate in Chapter 3, followed by a comprehensive characterization of the targets, in this Chapter, experimental validation of the benefits of the developed targes was investigated in a series of experiments.

4.1. Plasma plume imaging diagnostics at laser intensity of 10^{13} W/cm^2

The experiment was done irradiating the DLFT with a femtosecond pulsed laser with milli-joule (mJ) energy per pulse (with the Avesta Laser System) at ELI-NP. The targets' properties were evaluated through high-speed imaging of their interaction with the laser, focusing on the formation and ejection of the plasma plume at the target surface. Comparisons with measurements using bare Al foils under similar laser interactions revealed significant differences in plume generation, highlighting the potential for improved ion acceleration.

In order to investigate the interaction dynamics and potential benefits of the carbon foam coatings, we irradiated the DLFT and reference target of bare Al foils, with 70 fs laser pulses having sub-millijoule energies (~750 μJ), focused to a 160 μm spot and reaching peak intensities on the order of $10^{13} W/cm^2$. This intensity regime was selected to replicate the typical levels encountered in the prepulses or on the pedestal of high-power laser systems used for laser-driven particle acceleration. To investigate the spatial and temporal evolution of plasma plume emission, we employed fast-framing optical diagnostics using an intensified CCD (ICCD) camera, positioned perpendicular to the direction of plume expansion. The ICCD system was synchronized with the laser source to capture a single time-resolved image for each laser shot.

Carbon foam coatings were deposited by PLD in CH_4 at 1, 5, and 10 mbar. The deposition pressure influences the resulting foam microstructure and density: lower pressures led to denser films, while deposition at 10 mbar produced the most porous and spatially extended carbon networks, indicative of the lowest mass density.

Under these irradiation conditions, the focused laser pulses initiated surface ablation of the carbon foam or metallic substrate, followed by the ejection of a plasma plume. At this intensity and pulse duration, the laser–matter interaction was predominantly driven by nonlinear processes such as multiphoton ionization, with minimal thermal conduction due to the ultrashort pulse width.

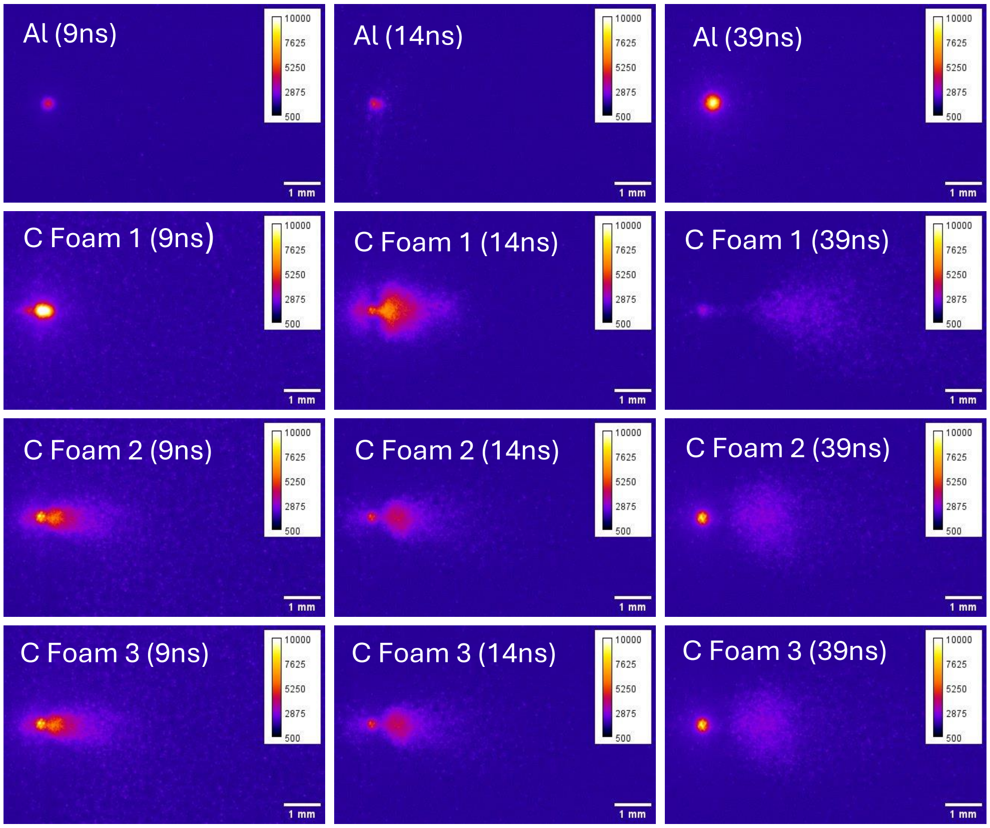

Figure 4.1. *ICCD images of plasma plume emission captured at three different time delays: 9 ns, 14 ns, and 39 ns—following the laser irradiation of bare aluminum foils (top row) and aluminum foils coated with carbon foams deposited with different* CH_4 *background gas conditions: C Foam 1 (1 mbar* CH_4*) C Foam 2 (5 mbar* CH_4*), and C Foam 3 (10 mbar* CH_4*).*

Figure 4.1. presents a comparative analysis of the plasma plume dynamics following laser irradiation of DLFT. C Foam 1 refers to the sample deposited at 1 mbar CH_4, C Foam 2 corresponds to 5 mbar CH_4 and C Foam 3 was fabricated under 10 mbar CH_4 background gas pressure. The images clearly demonstrate that, in all examined cases, the carbon foam-coated

targets exhibit a more extensive and rapidly expanding plasma plume compared to the conventional metallic targets.

At a temporal delay of 15 ns after the laser–target interaction, no detectable emission is observed from the bare Al foil, indicating that the plasma produced is either too weak or has already dissipated. In contrast, the target coated with C Foam 1 exhibits a well-developed, high-intensity plume, expanding over several millimetres and emitting bright optical radiation. While C Foam 2 and C Foam 3 also generate visible plasma plumes, these appear significantly dimmer and less extended than that produced by the denser C Foam 1.

This trend persists at longer delay times. At 40 ns post-irradiation, the bare Al foil no longer shows any observable plume activity, while the carbon foam-coated targets continue to emit light and expand outward into the vacuum. These observations strongly suggest that the carbon foam layer enhances laser energy absorption, likely due to its porous structure, increased effective surface area, and favorable absorption characteristics.

These results indicate that the porous carbon foam enhances laser absorption due to increased surface area and favorable optical properties, sustaining plasma even at intensities typical of prepulses (~10^{13} W/cm^2). Since such prepulses in CPA systems (~10^{21} W/cm^2 peak intensity, contrast 10^{-7}–10^{-8}) can strongly affect subsequent Target Normal Sheath Acceleration (TNSA), engineering foam density and thickness provides a means to control preplasma formation, promote self-focusing of the main pulse, and improve ion acceleration performance.

DLFT with carbon coatings thus act as engineered preplasma generators, offering new control parameters for optimizing laser–plasma interactions in high-intensity experiments.

4.2. Proton acceleration during the 1PW commissioning campaign at ELI-NP

This subchapter presents the experimental campaign conducted at the Extreme Light Infrastructure - Nuclear Physics (ELI-NP), during which double-layer foam targets (DLFTs) were successfully irradiated. The two experiments described here were performed during the commissioning phase of the 1 PW experimental area at ELI-NP. The first one aimed to evaluate the DLFT target compatibility in High Power Laser System (experiments) and the initial acceleration performance at sub-3 J laser energy, while the second one, conducted at full 1 PW power, focused on comparing the ion acceleration efficiency of DLFTs against conventional bare Al foil targets.

4.2.1. Proton acceleration at 10^{20} W/cm^2 Intensity regime

The first experiment was conducted with arm A in C1 interaction chamber, where the laser was focused directly on the DLFTs without the implementation of a plasma mirror between the off-axis parabolic mirror (OAP) and the target. In the absence of the PM, the primary objective of this preliminary DLFT irradiation was to assess the reliability of these novel targets safe use under laser irradiation, particularly regarding back reflection risks and vacuum chamber contamination.

The p-polarized beam was focused at 45° incidence using an f/3.7 OAP. To limit BR intensity, the laser energy was reduced to 2.7 J before the compressor (efficiency ~0.7), producing ~10^{20} W/cm^2 on target within a 3.9 × 4.0 µm FWHM focal spot. Targets consisted of DLFTs made of 7 µm carbon foam deposited on 1.5 µm and 3 µm Al foils. The foam was confined to 250 µm-radius discs (using a mask during the deposition) to minimize chamber contamination.

To determine contamination, the entire vacuum cycle was closely monitored and no anomalous outgassing or particulate contamination was detected during the entire pumping phase. After irradiation, detailed optical inspection of optical components (particularly the OAP), revealed no visible damage or material deposition. The absence of any carbonaceous residue confirmed that the structural integrity of the ultra-low density carbon layer had been maintained. These results demonstrate that, under the conditions tested, DLFTs do not represent a significant contamination risk to the optical infrastructure of the experimental setup.

Back-reflection was measured using a fast GaAs photodiode (30 ps rise time).

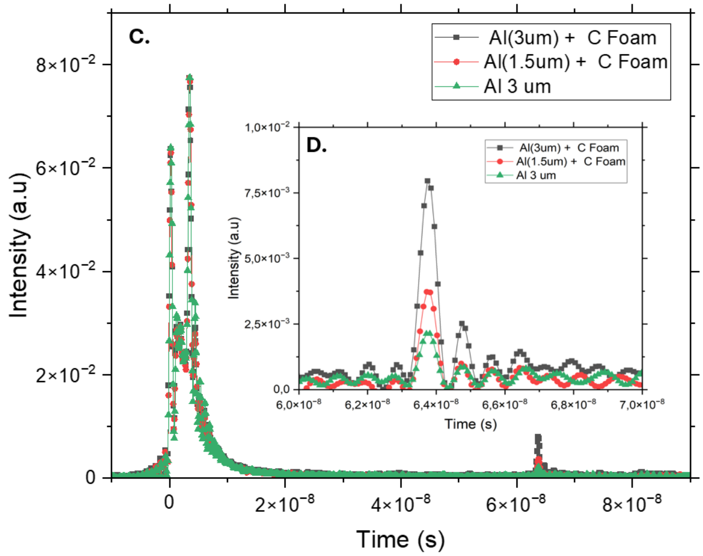

Figure 4.2. *Temporal profiles of back-reflected laser signals recorded via fast photodiode for three target configurations: DLFT with 3 µm Al + carbon foam (black squares), DLFT with 1.5 µm Al + carbon foam (red circles), and bare 3 µm Al foil (green triangles), (C) Full BR signal traces, (D) Zoomed view of the BR peak.*

Figure 4.2.. shows that the DLFT with 3 µm Al produced the strongest BR signal, followed by the 1.5 µm DLFT, while the bare 3 µm Al foil gave the lowest BR (three times smaller). This may indicate that the carbon foam modifies preplasma conditions, maintaining a more uniform critical surface at main-pulse arrival. Importantly, all BR levels remained below thresholds of concern for the HPLS monitoring system, confirming safe operation.

A key result of the experimental campaign was the successful observation of proton acceleration from DLFTs, measured using a radiochromic film (RCF) stack and a Thomson Parabola Spectrometer (TPS).

The RCF stack comprised 19 layers (11 HD-V2 + 8 EBT3, from Gafchromic [81]). Localized darkened features correspond to proton tracks, while diffuse uniform darkening is attributed to X-rays.

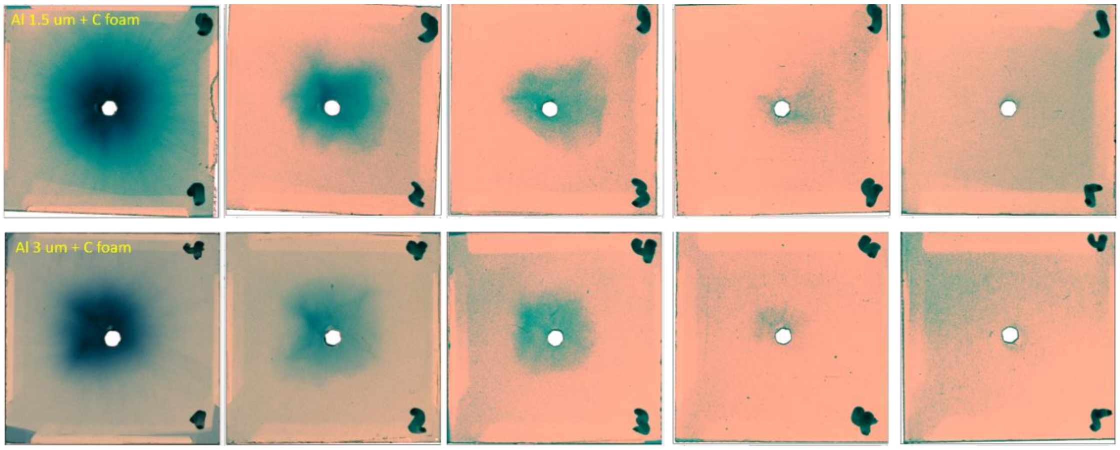

Figure 4.3. *Enhanced contrast analysis on the RCF stack response for two double-layer foam targets (DLFTs). The top row corresponds to the target with a 1.5 µm Al foil + 7 µm carbon foam (Stack 9), while the bottom row corresponds to the 3 µm Al + 7 µm carbon foam target (Stack 4). Each column represents a successive RCF layer, from front (left) to rear (right), showing the spatially resolved proton dose.*

Figure 4.3. shows the enhanced contrast response for two DLFTs: 1.5 µm Al + 7 µm C foam (top row, Stack 9) and 3 µm Al + 7 µm C foam (bottom row, Stack 4). In both cases, the first RCF layers display a central, circular proton imprint surrounded by a diffuse halo from X-rays/electrons. The signal weakens with depth, vanishing after the fourth layer, which corresponds to a proton cut-off energy of ~5.5 MeV. Beyond this, only diffuse background remains, confirming proton stopping.

The similar penetration depth, spatial profile, and intensity across the two stacks indicate nearly identical acceleration conditions for both DLFT configurations.

The TPS provided complementary spectral data, corroborating the RCF analysis.

Figure 4.4. presents proton spectra retrieved from calibrated image plates (IPs) using the Thomson Parabola Spectrometer (TPS), expressed as proton number per unit energy and steradian versus kinetic energy (MeV). Both spectra exhibit the exponential shape typical of TNSA.

Graph A corresponds to a DLFT made of 1.5 µm Al + 7 µm carbon foam, while Graph B shows results for 3 µm Al + 7 µm foam. In both cases, the yield is modest (~10^{10} protons/sr), consistent with the low laser energy delivered (<1 J on target). The slightly higher cutoff energy observed with the 3 µm Al foil is attributed to better rear-surface integrity, in agreement with the stronger BR signal recorded for this configuration.

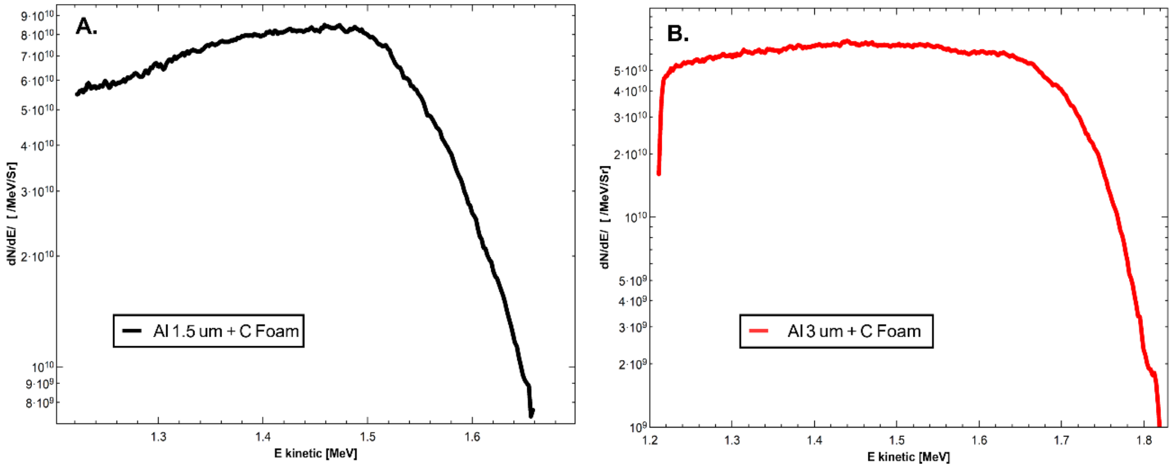

Figure 4.4. *Proton spectra retrieved from the raw data presented in the IP for the DLFT: A. Spectra from Al 1.5 µm + µm C Foam. B. Spectra from Al 3 µm + 7 µm C Foam.*

A discrepancy between proton cutoff energies measured by the TPS and those inferred from the RCF stack likely arises from a misalignment between the ion emission axis and the RCF aperture, which may have blocked the highest-energy protons before reaching the TPS pinhole.

4.2.2. Proton Acceleration at 2x10^{21} W/cm^2 Laser Intensity

The second campaign using DLFTs was performed in the C3 interaction chamber of the E5 area with arm B of the HPLS. The laser beam entered the chamber ~870 mm above the optical table and was focused using the same f/3.7 OAP at 45° incidence. Wavefront correction was achieved via adaptive optics (deformable mirror + wavefront sensor), yielding a focal spot of (3.9 ± 0.2) µm FWHM. The p-polarized beam impinged on the target at 25° ± 1° relative to normal.

To improve temporal contrast, a single plasma mirror (PM) was integrated into the beamline. The PM, consisting of an AR-coated substrate with λ/10 rms surface flatness, provided ~75% reflectivity at full power, effectively suppressing pre-pulses and pedestal contributions.

Two DLFT configurations were irradiated:1.5 µm Al foil + 40 µm C foam and 3 µm Al foil + 90 µm C foam. These thicker foam layers, compared to the first campaign, were designed to probe enhanced coupling and modified laser–plasma interaction dynamics

The primary diagnostic for characterizing ion acceleration was the stack of RCF, identical in configuration to that used in the first experiment. It was positioned at a distance of 25 mm behind the rear surface of the targets, thereby enabling accurate detection of the ion beam's angular distribution and energy deposition profile.

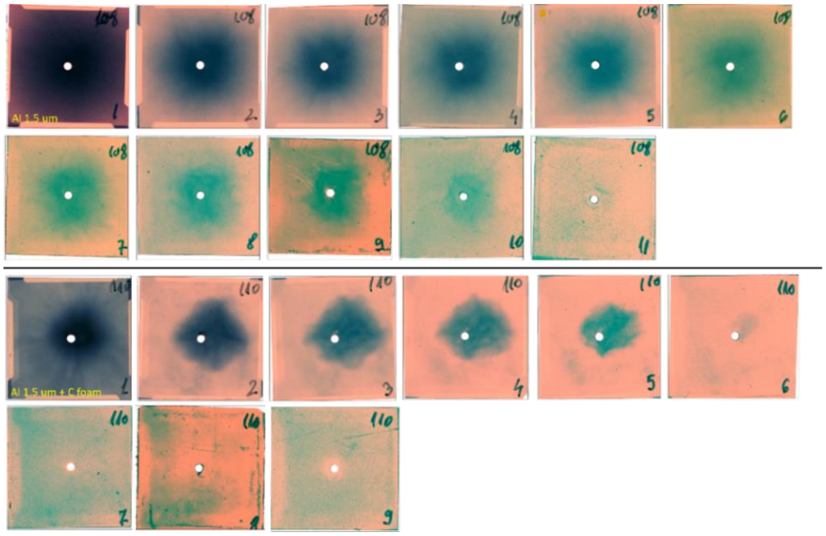

Figure 4.5. *Enhanced contrast analysis on the RCF stack response DLFT vs Al bare foil. The top row corresponds to a 1.5 µm Al bare foil target (Stack 108), while the bottom row corresponds to the 1.5 µm Al + 40 µm carbon foam target (Stack 110). Each column represents a successive RCF layer, from front (left) to rear (right), showing the spatially resolved proton dose.*

Figure 4.5 compares enhanced-contrast RCF responses for a bare 1.5 µm Al foil (Stack 108) and a DLFT (1.5 µm Al + 40 µm C foam, Stack 110). Successive layers reveal that protons from the bare Al foil penetrated up to the 10th layer, corresponding to a cut-off energy of ~18.6 MeV. By contrast, the DLFT signal extended only to the 6th layer, with a cut-off energy of ~9.7 MeV. Beyond these layers, only diffuse X-ray/electron background was visible.

The beam divergence was also inferred in Figure 4.. by analysing the size and evolution of the beam imprint across successive layers, with clear evidence on the lower divergence of the proton beam accelerated from the DLFT.

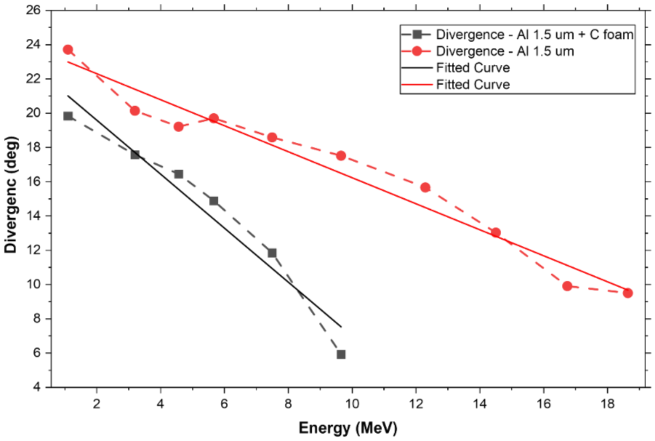

Figure 4.6. *Divergence of the proton beam as a function of kinetic energy for Al vs DLFTs: 1.5 µm Al (red) and 1.5µm Al + 40 µm C foam (black).*

Figure 4.6 provides a quantified analysis of the proton beam divergence as a function of kinetic energy, comparing the divergence characteristics for the two target configurations: bare 1.5 µm Al foil and DLFT (1.5 µm Al + 40 µm Carbon foam). The data clearly show that the proton beam generated from this DLFT exhibits a significantly lower divergence across the entire energy spectrum, indicating a more collimated beam profile compared to the beam accelerated from the bare Al foil. At a kinetic energy of 7.5 MeV, the divergence angle for the DLFT is approximately 12°, versus ~19° for bare Al. This trend becomes even more pronounced at higher energy, for DLFT at 9.7 MeV, the divergence narrowed further to ~6° (DLFT) compared to ~17.5° (bare Al).

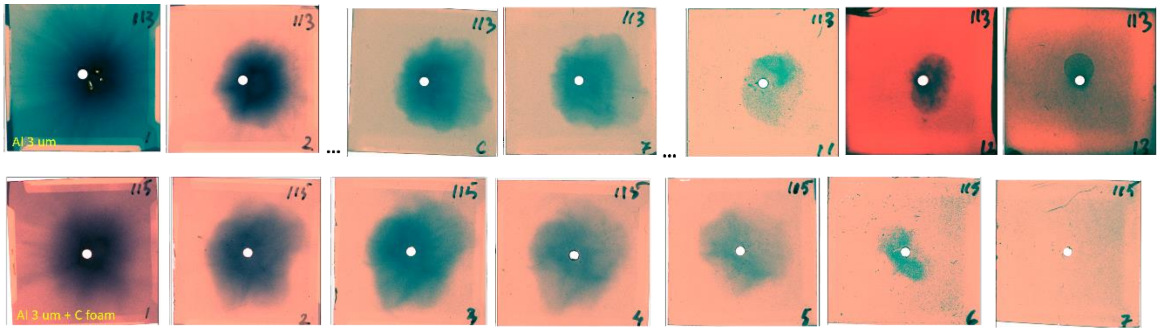

Figure 4.7. *Enhanced contrast analysis on the RCF stack response DLFT VS Al bare foil. The top row corresponds to a 3 µm Al bare foil target, while the bottom row corresponds to the 3 µm Al + 90 µm Carbon foam target. Each column represents a successive RCF layer, from front (left) to rear (right), showing the spatially resolved proton dose*

Figure 4.7. showed that for the bare 3 µm Al target, RCF layers revealed a spatially uniform proton beam across all irradiated depths. The final localized signal appeared on the 12th layer, corresponding to a cut-off energy of ~27.6 MeV. The apparent higher intensity on this layer arises from the transition from HD-V2 (layers 1–11) to the more sensitive EBT-3 films (layers ≥12). By the 13th layer, only diffuse background was observed, confirming full proton stopping.

In contrast, the DLFT (3 µm Al + 90 µm C foam) produced localized proton imprints only up to the 6th layer, corresponding to a cut-off energy of ~9.7 MeV. Beyond this depth, only diffuse background signals were visible. The reduced proton energy is attributed to the thick foam layer: although ultra-low density foams can enhance absorption and hot-electron generation, the 90 µm thickness likely introduced significant collisional losses and scattering, weakening the rear-side sheath field required for efficient TNSA.

The clear discrepancy in proton energy suggests a reduced acceleration performance from the DLFT configuration for this laser parameters. A likely explanation lies in the interaction of the laser pulse with the ultra-low-density carbon foam, which is ionised into a near-critical plasma. Because the foam layer is too thick (90 microns) it may also induce strong collisional losses and scattering within the foam, reducing the energy of the hot electrons before they reach the rear side diminishing the sheath field required for effective TNSA and consequently, the maximum energy of the accelerated protons

In terms of divergence, Figure 4.8. shows the same trend as Figure 4..:

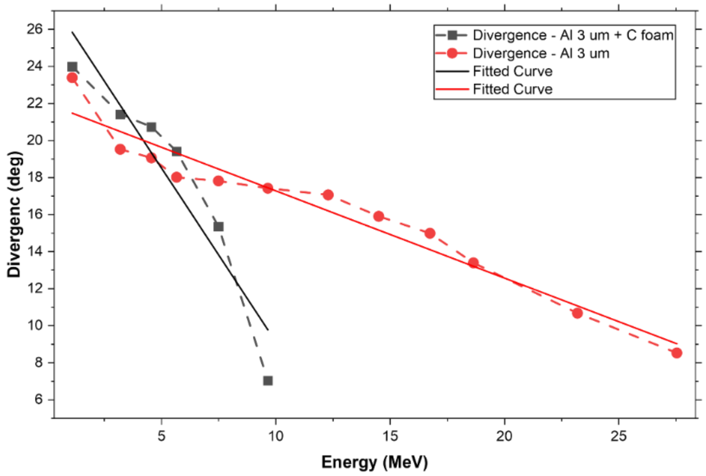

Figure 4.8. *Divergence of the proton beam as a function of kinetic energy for Al vs DLFTs: 3 Al (red) and 3 µmAl + 90 µm C foam (black).*

Figure 4.8. shows the divergence analysis, consistent with earlier results. The DLFT beam exhibits lower divergence across the energy spectrum compared to the bare Al foil, confirming that while DLFTs reduce maximum proton energy, they produce more collimated beams.

Consistent with the previous observations, the DLFT yields a proton beam with a significantly lower divergence, indicating a more collimated acceleration compared to the bare Al foil. This suggests that the DLFT configuration more effectively guides the fast electrons responsible for sheath field generation, resulting in a narrower angular spread of the accelerated proton beam.

In terms of energy, bare Al foils yielded higher proton cut-off values (19–27 MeV), while DLFTs typically reached only ~10 MeV. Despite this reduction, the enhanced collimation was observed for all foam thicknesses, pointing to modified electron transport in the near-critical plasma created by ionized foams. However, when the foam layer was excessively thick, collisional losses reduced the acceleration efficiency, both in proton number and maximum energy.

4.3. Enhanced proton acceleration with prepulse ionisation at Gemini, RAL

This experiment was conducted with the Astra-Gemini laser system at the Rutherford Appleton Laboratory (UK). The final amplifier delivered 17 ± 1 J pulses, with ~75% compressor efficiency, ~50% double plasma mirror (DPM) reflectivity, and ~80% transmission through steering optics, yielding an on-target energy of ~5.1 J. The beam was focused at normal incidence using an f/2 OAP, producing a 4.4 µm FWHM focal spot. With ~25% of the energy confined to this spot, the peak intensity reached $\sim 2 \times 10^{20}$ W/cm^2

During the experimental campaign, an unexpected discrepancy was observed between the anticipated and measured temporal contrast of the laser pulse. While the double plasma mirror (DPM) system was expected to enhance the temporal contrast to the level of $\sim 10^{-12}$ up to time delays of several hundred picoseconds, consistent with previous results [83] in situ measurements within the interaction chamber revealed the presence of a highly intense prepulse, 40 nanoseconds before the main pulse arrived. It was determined that the laser pre-pulse exhibited intensities of 10^{11}–10^{12} W/cm^2 after passing through the DPM system. This level of intensity corresponds to a prepulse with sufficient intensity to start ionising the low-density C foam layer prior to the arrival of the main pulse.

The target used were the DLFTs, each comprising a 15 µm low-density C foam layer deposited on Al foil substrates of varying thicknesses (0.4, 0.8, 1.5, 3, 6 and 10 µm).

Ion diagnostics included two Thomson Parabola Spectrometers (TPS) at 0° and 5° to capture angular dependence, and a Time-of-Flight (TOF) detector (pCVD diamond [84], 100 µm thick, 100 V bias) positioned at 4° relative to the laser axis for complementary proton detection.

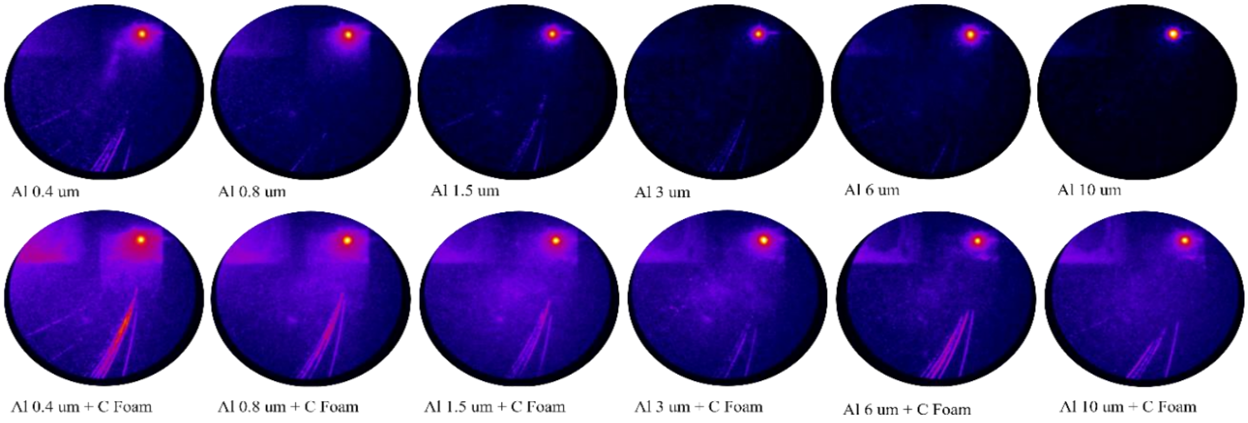

Figure 4.9. *Raw MCP images from the TPS at 0° relative to target normal. Top row: bare Al foils of thickness 0.4, 0.8, 1.5, 3, 6, and 10 µm. Bottom row: corresponding DLFTs with a 15 µm carbon foam layer deposited on Al substrates of identical thicknesses.*

Figure 4.10. presents the corresponding proton spectra (logarithmic scale) from the MCP/TPS data. For all substrate thicknesses (0.4–10 µm), DLFTs (red circles) consistently show broader distributions and higher apparent yields relative to bare Al foils (black squares). Although absolute proton numbers could not be extracted due to the lack of MCP calibration, the relative comparisons confirm superior acceleration with DLFTs.

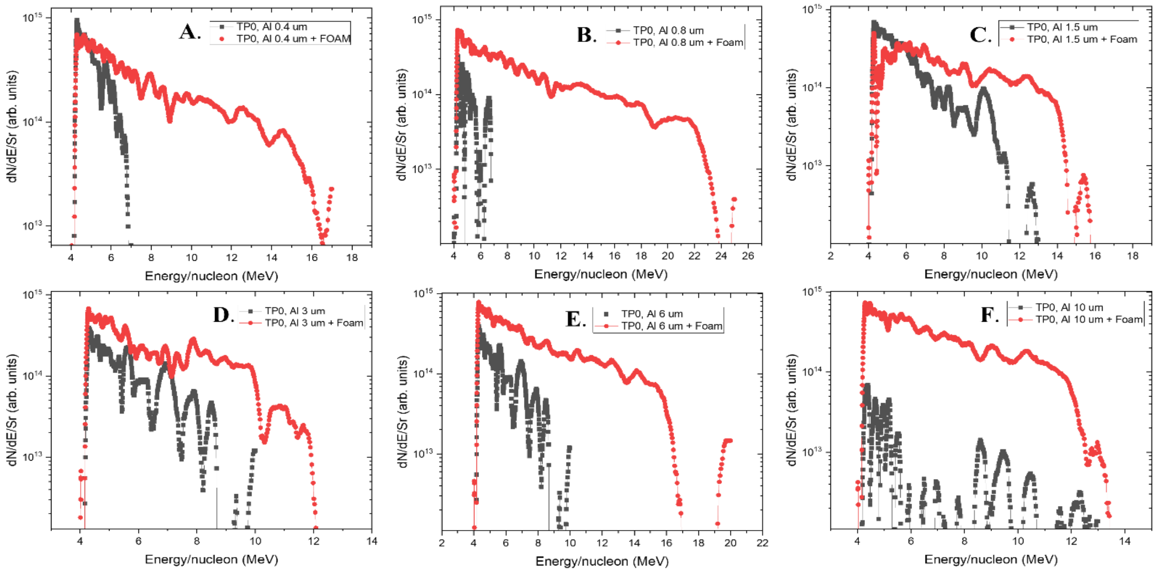

Figure 4.10. *Comparative proton energy spectra from the MCP at 0° TPS. Subplots (A–F) show logarithmic proton energy distributions (arbitrary units) for DLFTs (red circles) versus bare Al foils (black squares) at substrate thicknesses of (A) 0.4 µm, (B) 0.8 µm, (C) 1.5 µm, (D) 3 µm, (E) 6 µm, and (F) 10 µm.*

In all cases, the DLFTs exhibit both a broader energy distribution and a higher apparent proton yield relative to their bare Al analogues. This supports the hypothesis that the addition of a low-density carbon foam layer enhances sheath field formation and sustains stronger accelerating fields during proton acceleration.

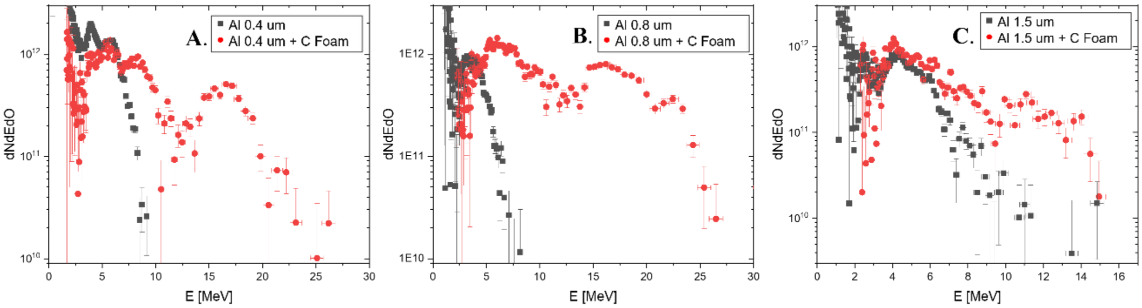

Figure 4.11. *Comparison of ion energy spectra obtained via TOF diagnostics for DLFTs (red circles) and bare Al foils (black squares) at different substrate thicknesses: (A) 0.4 µm, (B) 0.8 µm, and (C) 1.5 µm.*

Figure 4.11. presents the energy spectra of protons and ions obtained from the TOF measurements. Although the total number of protons could not be quantitatively determined due to spectral overlap with heavier ions, the cut-off energy of the proton was extracted. In all three cases, the TOF-based spectra confirm the trends observed from the TPS diagnostics: the DLFTs systematically yield higher proton cut-off energies than the corresponding bare Al foils.

Conclusions

The work presented in this thesis has demonstrated the successful design, fabrication, and experimental validation of double-layer foam targets (DLFTs) consisting of an ultra-low-density carbon foam deposited on aluminium substrates, specifically for the purpose of enhancing laser-driven proton acceleration. This general conclusion is supported by a sequence of intermediate findings that address target conception, material development, detailed characterisation, and systematic experimental testing under a variety of laser irradiation conditions.

At the conceptual stage, a comprehensive analysis of existing target types, including metallic foils, dielectric structures, and engineered composites, revealed that the most suitable target for the purpose of enhancing the acceleration of the protons would be a double layer foam target (DLFT) consisting of an ultra-low density (5-30 mg/cc) C foam layer (thicknesses in the micron-to-tens-of-micron range) on top of an Aluminium Layer (thicknesses from 0.4 to 10 µm) . The low-density structure should facilitate the formation of a controlled, near-critical plasma layer on the illuminated surface. This enables the laser pulse to penetrate deeper into the target, enhancing energy absorption within a larger plasma volume, which results in more efficient electron heating and improved ion acceleration conditions.

The carbon foams were fabricated using Pulsed Laser Deposition (PLD). Optimal results were achieved by using either N_2 or CH_4 as the background gas at a pressure of 1–10 mbar, which enhanced clustering and porosity formation.

Characterisation through gravimetry, n-RBS, SEM, and XPS confirmed the intended ultra-low-density (5–30 mg/cc), snowflake-like morphology, with typical void sizes of 1–5 µm. Deposited on solid aluminium layers, these DLFTs exhibited the structural and compositional features required for laser–plasma interaction studies.

The experimental studies validated the behaviour of these targets under different irradiation conditions. When exposed to femtosecond laser pulses with intensities around 10^{13} W/cm^2, comparable to the prepulse or pedestal of high-power laser systems, the DLFTs produced plasma plumes that were more intense, sustained, and spatially extended than those from bare aluminium foils. ICCD imaging confirmed that the foams supported long-lived plasma emission, demonstrating enhanced laser absorption and plasma coupling efficiency.

The first validation of DLFTs under high-power, high-intensity conditions was performed at ELI-NP using one arm of the 1 PW High Power Laser System (HPLS) at lower energy (~3J) at an intensity level of $10^{20} W/cm^2$. The targets demonstrated excellent vacuum compatibility throughout the pumping cycle and irradiation, with no evidence of optical contamination, particularly of the off-axis parabolic mirror. Back-reflection measurements indicated that DLFTs with 3 µm aluminium substrates produced stronger signals than those with thinner 1.5 µm substrates and bare foils, but these remained within safe operational limits even without plasma mirrors. Both target configurations (1.5 µm and 3 µm Al with 7 µm foam) generated measurable proton acceleration via the target normal sheath acceleration (TNSA) mechanism. Proton tracks extended to the fourth layer of RCF stacks, corresponding to cut-off energies of ~5.5 MeV, while spectra from the Thomson Parabola Spectrometer (TPS) suggested lower cut-off energies (~1.8 MeV) due to geometrical acceptance effects and possible misalignments.

In a subsequent experiment using the second arm of the HPLS at full power and 2×10^{21} W/cm² intensity, two DLFTs (1.5 µm Al + 40 µm foam and 3 µm Al + 90 µm foam) were compared with bare aluminium foils of the same thickness. While the bare foils achieved higher maximum proton energies (~18.6 MeV for 1.5 µm and ~27.6 MeV for 3 µm), the DLFTs produced more collimated proton beams, with divergence angles reduced to ~6° compared to ~17° for bare foils. This improved beam quality is attributed to the near-critical-density plasma formed in the foam, which channels electron transport and generates a more localised sheath field. However, very thick foam layers (40–90 µm) were shown to reduce acceleration efficiency, likely due to electron scattering and energy losses before reaching the rear surface.

The final experimental validation was performed at the Astra-Gemini laser system at the Rutherford Appleton Laboratory. Despite employing a double plasma mirror (DPM), the system exhibited a significant pre-pulse ~40 ns before the main pulse, with intensities of 10^{11}–10^{12} W/cm². This pre-pulse was sufficient to pre-ionise the carbon foam layer of the DLFTs, which in turn strongly enhanced the coupling efficiency of the subsequent main pulse. Across a wide range of aluminium substrate thicknesses (0.4–10 µm), the presence of the carbon foam consistently and significantly improved proton acceleration compared to bare foils. DLFTs yielded higher cut-off energies and greater proton fluxes as observed by both TPS and TOF diagnostics. Particularly striking improvements were seen for very thin (0.4 and 0.8 µm) and very thick (6 and 10 µm) substrates. For example, with 0.4 µm Al, DLFTs achieved cut-off energies of ~25 MeV compared to ~8 MeV for bare foils, while for 10 µm Al, DLFTs still produced protons up to ~14 MeV whereas bare foils gave negligible signals.

Overall, these results demonstrate that DLFTs provide clear advantages under a range of irradiation conditions. Although they do not always yield the highest maximum proton energies, their ability to enhance laser absorption, sustain preplasma, reduce beam divergence, and exploit the beneficial effects of pre-pulses establishes them as a robust and versatile target design for laser–plasma interaction studies. The work presented here, from design to fabrication, characterisation, and high-intensity laser irradiation, confirms the viability of DLFTs as engineered targets for optimising laser-driven proton acceleration.

Bibliography

[1] D. Strickland and G. Mourou, “Compression of amplified chirped optical pulses,” *Opt. Commun.*, vol. 56, no. 3, pp. 219–221, Dec. 1985, doi: 10.1016/0030-4018(85)90120-8.

[2] G. A. Mourou, T. Tajima, and S. V. Bulanov, “Optics in the relativistic regime,” *Rev. Mod. Phys.*, vol. 78, no. 2, pp. 309–371, Apr. 2006, doi: 10.1103/RevModPhys.78.309.

[3] H. Daido, M. Nishiuchi, and A. S. Pirozhkov, “Review of laser-driven ion sources and their applications,” *Rep. Prog. Phys.*, vol. 75, no. 5, p. 056401, Apr. 2012, doi: 10.1088/0034-4885/75/5/056401.

[4] R. A. Snavely *et al.*, “Intense high-energy proton beams from petawatt-laser irradiation of solids,” *Phys. Rev. Lett.*, vol. 85, no. 14, pp. 2945–2948, 2000, doi: 10.1103/PhysRevLett.85.2945.

[5] A. Higginson *et al.*, “Near-100 MeV protons via a laser-driven transparency-enhanced hybrid acceleration scheme,” *Nat. Commun.*, vol. 9, no. 1, p. 724, 2018, doi: 10.1038/s41467-018-03063-9.

[6] T. Ziegler *et al.*, “Laser-driven high-energy proton beams from cascaded acceleration regimes,” *Nat. Phys.*, vol. 20, no. 7, pp. 1211–1216, Jul. 2024, doi: 10.1038/s41567-024-02505-0.

[7] C. Radier *et al.*, “10 PW peak power femtosecond laser pulses at ELI-NP,” *High Power Laser Sci. Eng.*, vol. 10, p. e21, Jan. 2022, doi: 10.1017/hpl.2022.11.

[8] B. Rus *et al.*, “ELI-beamlines: progress in development of next generation short-pulse laser systems,” in *Research Using Extreme Light: Entering New Frontiers with Petawatt-Class Lasers III*, SPIE, Jun. 2017, pp. 14–21. doi: 10.1117/12.2269818.

[9] S. Kühn *et al.*, “The ELI-ALPS facility: the next generation of attosecond sources,” *J. Phys. B At. Mol. Opt. Phys.*, vol. 50, no. 13, p. 132002, Jun. 2017, doi: 10.1088/1361-6455/aa6ee8.

[10] C. B. Edwards *et al.*, “Vulcan upgrade: a petawatt laser facility for experiments at 1021 Wcm-2,” in *ECLIM 2000: 26th European Conference on Laser Interaction with Matter*, SPIE, Apr. 2001, pp. 63–69. doi: 10.1117/12.425537.

[11] K. Burdonov *et al.*, “Characterization and performance of the Apollon short-focal-area facility following its commissioning at 1 PW level,” *Matter Radiat. Extrem.*, vol. 6, no. 6, p. 064402, Oct. 2021, doi: 10.1063/5.0065138.

[12] Z. Major *et al.*, “High-energy laser facility PHELIX at GSI: latest advances and extended capabilities,” *High Power Laser Sci. Eng.*, vol. 12, p. e39, Jan. 2024, doi: 10.1017/hpl.2024.17.

[13] J. W. Yoon *et al.*, “Realization of laser intensity over 10^{23} W/cm^2,” *Optica*, vol. 8, no. 5, pp. 630–635, May 2021, doi: 10.1364/OPTICA.420520.

[14] H. Kiriyama *et al.*, “Recent Progress on an Upgrade of the J-KAREN Laser at JAEA,” in *2015 Conference on Lasers and Electro-Optics Pacific Rim (2015), paper 26D2_2*, Optica Publishing Group, Aug. 2015, p. 26D2_2. Accessed: 2025. [Online]. Available: https://opg.optica.org/abstract.cfm?uri=CLEOPR-2015-26D2_2

[15] L. Obst-Huebl *et al.*, “High power commissioning of BELLA iP2 up to 17 J,” in *Applying Laser-driven Particle Acceleration III: Using Distinctive Energetic Particle and Photon Sources*, SPIE, Jun. 2023, pp. 19–25. doi: 10.1117/12.2669162.

[16] I. Prencipe *et al.*, “Targets for high repetition rate laser facilities: needs, challenges and perspectives,” *High Power Laser Sci. Eng.*, vol. 5, p. e17, 2017, doi: 10.1017/hpl.2017.18.

[17] I. Langmuir, “Oscillations in Ionized Gases,” *Proc. Natl. Acad. Sci. U. S. A.*, vol. 14, no. 8, pp. 627–637, Aug. 1928, doi: 10.1073/pnas.14.8.627.

[18] R. N. Franklin and N. S. J. Braithwaite, “80 Years of Plasma,” *Plasma Sources Sci. Technol.*, vol. 18, no. 1, p. 010201, Feb. 2009, doi: 10.1088/0963-0252/18/1/010201.

[19] F. F. Chen, *Introduction to Plasma Physics and Controlled Fusion*. Springer, 1984.

[20] P. Mulser, R. Sigel, and S. Witkowski, "Plasma production by laser," *Phys. Rep.*, vol. 6, no. 3, pp. 187–239, Jan. 1973, doi: 10.1016/0370-1573(73)90005-7.

[21] A. Seryi, *Unifying Physics of Accelerators, Lasers and Plasma*. CRC Press, 2015.

[22] M. Borghesi, "Laser-driven ion acceleration: State of the art and emerging mechanisms," *Nucl. Instrum. Methods Phys. Res. Sect. Accel. Spectrometers Detect. Assoc. Equip.*, vol. 740, pp. 6–9, Mar. 2014, doi: 10.1016/j.nima.2013.11.098.

[23] H. Padamsee, J. Knobloch, and T. Hays, *RF Superconductivity for Accelerators*. John Wiley & Sons, 2008.

[24] S. J. Gitomer, R. D. Jones, F. Begay, A. W. Ehler, J. F. Kephart, and R. Kristal, "Fast ions and hot electrons in the laser–plasma interaction," *Phys. Fluids*, vol. 29, no. 8, pp. 2679–2688, Aug. 1986, doi: 10.1063/1.865510.

[25] M. Roth and M. Schollmeier, "Ion acceleration—target normal sheath acceleration," in *Proceedings of the CAS-CERN Accelerator School: Plasma Wake Acceleration,* B. Holzer, Ed., SPIE, 2016.

[26] A. Macchi, M. Borghesi, and M. Passoni, "Ion acceleration by superintense laser-plasma interaction," *Rev. Mod. Phys.*, vol. 85, no. 2, pp. 751–793, 2013, doi: 10.1103/RevModPhys.85.751.

[27] A. J. Mackinnon *et al.*, "Enhancement of Proton Acceleration by Hot-Electron Recirculation in Thin Foils Irradiated by Ultraintense Laser Pulses," *Phys. Rev. Lett.*, vol. 88, no. 21, p. 215006, May 2002, doi: 10.1103/PhysRevLett.88.215006.

[28] D. Neely *et al.*, "Enhanced proton beams from ultrathin targets driven by high contrast laser pulses," *Appl. Phys. Lett.*, vol. 89, no. 2, p. 021502, Jul. 2006, doi: 10.1063/1.2220011.

[29] D. Batani *et al.*, "Effects of laser prepulses on laser-induced proton generation," *New J. Phys.*, vol. 12, no. 4, p. 045018, Apr. 2010, doi: 10.1088/1367-2630/12/4/045018.

[30] A. Flacco *et al.*, "Comparative study of laser ion acceleration with different contrast enhancement techniques," *Nucl. Instrum. Methods Phys. Res. Sect. Accel. Spectrometers Detect. Assoc. Equip.*, vol. 620, no. 1, pp. 18–22, Aug. 2010, doi: 10.1016/j.nima.2010.01.053.

[31] M. Kaluza *et al.*, "Influence of the laser prepulse on proton acceleration in thin-foil experiments," *Phys. Rev. Lett.*, vol. 93, no. 4, p. 045003, 2004, doi: 10.1103/PhysRevLett.93.045003.

[32] L. A. Gizzi *et al.*, "Enhanced laser-driven proton acceleration via improved fast electron heating in a controlled pre-plasma," *Sci. Rep.*, vol. 11, no. 1, p. 13728, Jul. 2021, doi: 10.1038/s41598-021-93011-3.

[33] F. Quéré and H. Vincenti, "Reflecting petawatt lasers off relativistic plasma mirrors: a realistic path to the Schwinger limit," *High Power Laser Sci. Eng.*, vol. 9, p. e6, Jan. 2021, doi: 10.1017/hpl.2020.46.

[34] T. Chapman *et al.*, "Investigation and modeling of optics damage in high-power laser systems caused by light backscattered in plasma at the target," *J. Appl. Phys.*, vol. 125, no. 3, p. 033101, Jan. 2019, doi: 10.1063/1.5070066.

[35] M. C. Downer, R. Zgadzaj, A. Debus, U. Schramm, and M. C. Kaluza, "Diagnostics for plasma-based electron accelerators," *Rev. Mod. Phys.*, vol. 90, no. 3, p. 035002, Aug. 2018, doi: 10.1103/RevModPhys.90.035002.

[36] A. Boné, N. Lemos, G. Figueira, and J. M. Dias, "Quantitative shadowgraphy for laser–plasma interactions," *J. Phys. Appl. Phys.*, vol. 49, no. 15, p. 155204, Mar. 2016, doi: 10.1088/0022-3727/49/15/155204.

[37] A. Sävert *et al.*, "Direct Observation of the Injection Dynamics of a Laser Wakefield Accelerator Using Few-Femtosecond Shadowgraphy," *Phys. Rev. Lett.*, vol. 115, no. 5, p. 055002, Jul. 2015, doi: 10.1103/PhysRevLett.115.055002.

[38] A. Măgureanu *et al.*, "Target Characteristics Used in Laser-Plasma Acceleration of Protons Based on the TNSA Mechanism," *Front. Phys.*, vol. 10, Mar. 2022, doi: 10.3389/fphy.2022.727718.

[39] K. Flippo *et al.*, "Multi-MeV ion beams from terawatt laser thin-foil interactions," in *Proceedings of the IEEE Particle Accelerator Conference*, Conf.Proc.C 0106181 (2001) 2081-2083, 2001. doi: 10.1109/PAC.2001.987283.

[40] E. L. Clark *et al.*, “Measurements of energetic proton transport through magnetized plasma from intense laser interactions with solids,” *Phys. Rev. Lett.*, vol. 84, no. 4, pp. 670–673, 2000, doi: 10.1103/PhysRevLett.84.670.

[41] A. Maksimchuk, S. Gu, K. Flippo, D. Umstadter, and V. Y. Bychenkov, “Forward ion acceleration in thin films driven by a high-intensity laser,” *Phys. Rev. Lett.*, vol. 84, no. 18, pp. 4108–4111, 2000, doi: 10.1103/PhysRevLett.84.4108.

[42] M. Zepf *et al.*, “Fast particle generation and energy transport in laser-solid interactions,” *Phys. Plasmas*, vol. 8, no. 5, pp. 2323–2330, 2001, doi: 10.1063/1.1351824.

[43] K. A. Flippo, J. Workman, D. C. Gautier, S. Letzring, R. P. Johnson, and T. Shimada, “Scaling laws for energetic ions from the commissioning of the new LOS ALAMO NATlONAL LABORATORY 200 TW TRIDENT LASER,” *Rev. Sci. Instrum.*, vol. 79, no. 10, 2008, doi: 10.1063/1.2987678.

[44] F. Wagner *et al.*, “Maximum Proton Energy above 85 MeV from the Relativistic Interaction of Laser Pulses with Micrometer Thick CH2 Targets,” *Phys. Rev. Lett.*, vol. 116, no. 20, pp. 205002–205006, 2016, doi: 10.1103/PhysRevLett.116.205002.

[45] P. McKenna *et al.*, “Characterization of proton and heavier ion acceleration in ultrahigh-intensity laser interactions with heated target foils,” *Phys. Rev. E*, vol. 70, no. 3, p. 036405, 2004, doi: 10.1103/PhysRevE.70.036405.

[46] K. Ogura *et al.*, “Proton acceleration to 40 MeV using a high intensity, high contrast optical parametric chirped-pulse amplification Ti:sapphire hybrid laser system,” *Opt. Lett.*, vol. 37, no. 14, pp. 28682–2870, 2012, doi: https://doi.org/10.1364/OL.37.002868.

[47] T. P. Frazer *et al.*, “Enhanced laser intensity and ion acceleration due to self-focusing in relativistically transparent ultrathin targets,” *Phys. Rev. Res.*, vol. 2, no. 4, p. 042015, 2020, doi: 10.1103/PhysRevResearch.2.042015.

[48] S. P. Hatchett *et al.*, “Electron, photon, and ion beams from the relativistic interaction of Petawatt laser pulses with solid targets,” *Phys. Plasmas*, vol. 7, no. 5, pp. 2076–2082, 2000, doi: 110.1063/1.874030.

[49] Y. Murakami *et al.*, “Observation of proton rear emission and possible gigagauss scale magnetic fields from ultra-intense laser illuminated plastic target,” *Phys. Plasmas*, vol. 8, no. 9, pp. 4138–4143, 2001, doi: 10.1063/1.1390333.

[50] J. Hornung *et al.*, “Enhancement of the laser-driven proton source at PHELIX,” *High Power Laser Sci. Eng.*, vol. 08, p. e24, 2020, doi: 10.1017/hpl.2020.23.

[51] S. Okihara *et al.*, “Energetic proton generation in a thin plastic foil irradiated by intense femtosecond lasers,” *J. Nucl. Sci. Technol.*, vol. 39, no. 1, pp. 1–5, 2002, doi: 10.1080/18811248.2002.9715150.

[52] S. Ter-Avetisyan and P. V. Nickles, “Ion acceleration at the front and rear surfaces of thin foils with high-intensity 40-fs laser pulses,” *J. Exp. Theor. Phys. Lett.*, vol. 83, no. 5, pp. 206–210, 2006, doi: 10.1134/S0021364006050055.

[53] T. Ceccotti *et al.*, “Proton acceleration with high-intensity ultrahigh-contrast laser pulses,” *Phys. Rev. Lett.*, vol. 99, no. 18, p. 185002, 2007, doi: doi/10.1103/PhysRevLett.99.185002.

[54] F. Dollar *et al.*, “Finite spot effects on radiation pressure acceleration from intense high-contrast laser interactions with thin targets,” *Phys. Rev. Lett.*, vol. 108, no. 17, pp. 175005–175010, 2012, doi: 10.1103/PhysRevLett.108.175005.

[55] V. Floquet *et al.*, “Micro-sphere layered targets efficiency in laser driven proton acceleration,” *J. Appl. Phys.*, vol. 114, no. 8, p. 083305, 2013, doi: 10.1063/1.4819239.

[56] D. Margarone *et al.*, “Laser-driven high-energy proton beam with homogeneous spatial profile from a nanosphere target,” *Phys. Rev. Spec. Top. - Accel. Beams*, vol. 18, no. 7, p. 071304, Jul. 2015, doi: 10.1103/PhysRevSTAB.18.071304.

[57] A. Yogo *et al.*, “Laser ion acceleration via control of the near-critical density target,” *Phys. Rev. E*, vol. 77, no. 1, p. 016401, 2008, doi: 10.1103/PhysRevE.77.016401.

[58] L. Giuffrida *et al.*, “Nano and micro structured targets to modulate the spatial profile of laser driven proton beams,” *J. Instrum.*, vol. 12, no. 03, 2017, doi: 10.1088/1748-0221/12/03/c03040.

[59] A. M. Ilvenny *et al.*, "Characteristics of ion beams generated in the interaction of ultra-short laser pulses with ultra-thin foils," *Plasma Phys. Control. Fusion*, vol. 62, no. 5, p. 054001, 2020, doi: 10.1088/1361-6587/ab7d26.

[60] S. Palaniyappan *et al.*, "Efficient quasi-monoenergetic ion beams from laser-driven relativistic plasmas," *Nat. Commun.*, vol. 6, no. 1, p. 10170, 2015, doi: 10.1038/ncomms10170.

[61] P. L. Poole *et al.*, "Laser-driven ion acceleration via target normal sheath acceleration in the relativistic transparency regime," *New J. Phys.*, vol. 20, no. 1, p. 013019, 2018, doi: 10.1088/1367-2630/aa9d47.

[62] T. Ebert *et al.*, "Enhanced brightness of a laser-driven x-ray and particle source by microstructured surfaces of silicon targets," *Phys. Plasmas*, vol. 27, no. 4, p. 043106, 2020, doi: 10.1063/1.5125775.

[63] S. Fourmaux *et al.*, "Investigation of laser-driven proton acceleration using ultra-short, ultra-intense laser pulses," *Phys. Plasmas*, vol. 20, p. 013110, 2013, doi: 10.1063/1.4789748.

[64] W. J. Ma *et al.*, "Laser Acceleration of Highly Energetic Carbon Ions Using a Double-Layer Target Composed of Slightly Underdense Plasma and Ultrathin Foil," *Phys. Rev. Lett.*, vol. 122, no. 1, p. 014803, Jan. 2019, doi: 10.1103/PhysRevLett.122.014803.

[65] I. Prencipe *et al.*, "Development of foam-based layered targets for laser-driven ion beam production," *Plasma Phys. Control. Fusion*, vol. 58, no. 3, p. 034019, 2016, doi: 10.1088/0741-3335/58/3/034019.

[66] J. S. Green *et al.*, "High efficiency proton beam generation through target thickness control in femtosecond laser-plasma interactions," *Appl. Phys. Lett.*, vol. 104, no. 21, p. 214101, 2014, doi: 10.1063/1.4879641.

[67] L. Volpe *et al.*, "Generation of high energy laser-driven electron and proton sources with the 200 TW system VEGA 2 at the Centro de Laseres Pulsados," *High Power Laser Sci. Eng.*, vol. 7, pp. e25-1/6, 2019, doi: 10.1017/hpl.2019.10.

[68] F. Lindau *et al.*, "Laser-accelerated protons with energy-dependent beam direction," *Phys. Rev. Lett.*, vol. 95, no. 17, p. 175002, 2005, doi: 10.1103/PhysRevLett.95.175002.

[69] A. Flacco *et al.*, "Dependence on pulse duration and foil thickness in high-contrast-laser proton acceleration," *Phys. Rev. E*, vol. 81, no. 3, p. 036405, 2010, doi: 10.1103/PhysRevE.81.036405.

[70] S. Vallières *et al.*, "Enhanced laser-driven proton acceleration using nanowire targets," *Sci. Rep.*, vol. 11, no. 1, p. 2226, Jan. 2021, doi: 10.1038/s41598-020-80392-0.

[71] G. Cantono *et al.*, "Laser-driven proton acceleration from ultrathin foils with nanoholes," *Sci. Rep.*, vol. 11, no. 1, p. 5006, 2021, doi: 10.1038/s41598-021-84264-z.

[72] L. A. Gizzi *et al.*, "Intense proton acceleration in ultrarelativistic interaction with nanochannels," *Phys. Rev. Res.*, vol. 2, no. 3, pp. 033451–033456, 2020, doi: 10.1103/PhysRevResearch.2.033451.

[73] D. Margarone *et al.*, "Laser-driven proton acceleration enhancement by nanostructured foils," *Phys. Rev. Lett.*, vol. 109, pp. 234801–234806, 2012, doi: 10.1103/PhysRevLett.109.234801.

[74] I. Prencipe *et al.*, "Efficient laser-driven proton and bremsstrahlung generation from cluster-assembled foam targets," *New J. Phys.*, vol. 23, no. 9, p. 093015, Sep. 2021, doi: 10.1088/1367-2630/ac1fcd.

[75] A. V. Rode, S. T. Hyde, E. G. Gamaly, R. G. Elliman, D. R. McKenzie, and S. Bulcock, "Structural analysis of a carbon foam formed by high pulse-rate laser ablation," *Appl. Phys. Mater. Sci. Process.*, vol. 69, no. 7, pp. S755–S758, Dec. 1999, doi: 10.1007/s003390051522.

[76] A. V. Rode, E. G. Gamaly, and B. Luther-Davies, "Formation of cluster-assembled carbon nano-foam by high-repetition-rate laser ablation," *Appl. Phys. Mater. Sci. Process.*, vol. 70, no. 2, pp. 135–144, Feb. 2000, doi: 10.1007/s003390050025.

[77] A. Zani, D. Dellasega, V. Russo, and M. Passoni, "Ultra-low density carbon foams produced by pulsed laser deposition," *Carbon*, vol. 56, pp. 358–365, May 2013, doi: 10.1016/j.carbon.2013.01.029.

[78] A. Maffini, A. Pazzaglia, D. Dellasega, V. Russo, and M. Passoni, "Growth dynamics of pulsed laser deposited nanofoams," *Phys. Rev. Mater.*, vol. 3, no. 8, p. 083404, Aug. 2019, doi: 10.1103/PhysRevMaterials.3.083404.

[79] F. Guzmán *et al.*, “Pulsed laser deposition of thin carbon films in a neutral gas background,” *J. Phys. Appl. Phys.*, vol. 46, no. 21, p. 215202, May 2013, doi: 10.1088/0022-3727/46/21/215202.

[80] A. Usman *et al.*, “Impact of Argon gas on optical and electrical properties of Carbon thin films,” *Phys. B Condens. Matter*, vol. 503, pp. 157–161, Dec. 2016, doi: 10.1016/j.physb.2016.09.029.

[81] S. N. Chen *et al.*, “Absolute dosimetric characterization of Gafchromic EBT3 and HDv2 films using commercial flat-bed scanners and evaluation of the scanner response function variability,” *Rev. Sci. Instrum.*, vol. 87, no. 7, p. 073301, Jul. 2016, doi: 10.1063/1.4954921.

[82] M. O. Cernaianu *et al.*, “Commissioning of the 1 PW experimental area at ELI-NP using a short focal parabolic mirror for proton acceleration,” *Matter Radiat. Extrem.*, vol. 10, no. 2, p. 027204, Mar. 2025, doi: 10.1063/5.0241077.

[83] A. Lévy *et al.*, “Double plasma mirror for ultrahigh temporal contrast ultraintense laser pulses,” *Opt. Lett.*, vol. 32, no. 3, pp. 310–312, Feb. 2007, doi: 10.1364/ol.32.000310.

[84] “CIVIDEC Instrumentation - CVD Diamond Technology applications.” Accessed: 2025. [Online]. Available: https://cividec.at/index.php?module=public.product&idProduct=12&scr=0